Title

Modeling the topography of the salar de Uyuni, Bolivia as an equipotential surface of Earth's gravity field

Journal

Journal of Geophysical Research, 113(B10408)

ISSN

0148-0227

Author

Borsa, Adrian

Publication Date

2008-10-31

DOI

10.1029/2007JB005445

Peer reviewed

Modeling the topography of the salar de Uyuni, Bolivia as an equipotential surface of Earth's gravity field

Adrian A. Borsa[1], Bruce G. Bills[2], Jean-Bernard Minster[1]

[1]Institute of Geophysics and Planetary Physics, Scripps Institution of Oceanography, University of California at San Diego, La Jolla, California, USA
[2]Planetary Geodynamics Laboratory, NASA Goddard Space Flight Center, Greenbelt, Maryland, USA

ABSTRACT

The salar de Uyuni is a massive dry salt lake that lies at the lowest point of an internal-drainage basin in the Bolivian Altiplano. A kinematic GPS survey of the salar in September, 2002 found a topographic range of only 80 cm over a 54 x 45 km area and subtle surface features that appeared to correlate with mapped gravity. In order to confirm the correlation between topography and gravity/geopotential, we use local gravity measurements and the EGM96 global geopotential model to construct a centimeter-level equipotential surface corresponding to the elevation of the salar. Our comparison of GPS survey elevations with the equipotential surface estimate shows that 63% of the variance of the GPS elevations can be explained by equipotential surface undulations (and long-wavelength error) in the EGM96 model alone, with an additional 30% explained by the shorter-wavelength equipotential surface derived from local gravity. In order to establish a physical connection between topography and the geopotential, we also develop and test a simple surface process model that redistributes salt via the dissolution, transport and redeposition of salt by precipitated water. Forcing within the model pushes the system to evolve toward constant water depth, with the salt surface approximating the shape of the local equipotential surface. Since the model removes almost all topographic relief with respect to the equipotential surface within a matter of decades, it appears that observed (~5 cm

amplitude, ~5 km wavelength) residual topography is actively maintained by a process independent of gravity-driven fluid flow.

1. INTRODUCTION

Geomorphological studies of salt flats have typically focused on the sub-meter-scale response of the salt surface to rainwater associated with the annual hydrological cycle [e.g., *Lowenstein and Hardie*, 1985; *Sonnenfeld*, 1984]. Although this body of work carefully considers how the local crystalline structure of the salt changes in response to inundation and evaporation, it does not examine how small-scale processes might impact the shape of the overall surface. Also unaddressed is the more fundamental question of why salt flats are topographically flat over large areas, despite the fact that they often occur in tectonically active environments with considerable geomorphic forcing evident in the surrounding topography.

The most rigorous published description of salt flat topography appears to be that given by Warren [1989], which describes a salt flat as "an equilibrium geomorphic surface whose level is dictated by the local water table." Since the near-surface water table beneath most salt flats is a level surface of earth's geopotential field, this statement implies that a salt flat is such a surface as well. Warren, however, does not discuss how the water table enforces the leveling of the surface or just how level we should expect the surface to be. These questions are relevant to the scientific understanding of salt flat geomorphology as well as to the use of salt flats as reference surfaces for satellite altimeter calibration and validation [*Fricker et al.*, 2005], both of which require knowledge about the shape of the surface and the approximate time scale over which that shape might be expected to change.

The salar de Uyuni is a 9000 km^2 salt flat located high in the Bolivian Altiplano (Figure 1) whose halite surface was mapped by kinematic GPS in 2002 [*Borsa et al.*, 2008]. The 2002 survey showed the salar to be remarkably flat – 80 cm total relief over an area of 54 x 45 km – even though it occurs in an environment with active forcing due to tectonics and isostatic rebound [e.g. *Bills et al.*, 1994; *McGeary et al.*, 2003]. Furthermore, the subtle long-wavelength topography that does exist on the salar appears to be spatially correlated with the local gravity field. Since the salar has a near-surface water table and is regularly inundated by a shallow wet-season lake, one possibility is that its surface resembles the equipotential surface to which the water table conforms – an outcome that would explain both the overall flatness of the surface and its correlation with mapped gravity.

We test this hypothesis about the shape of salar topography by constructing a centimeter-level estimate of the local equipotential surface from gravity observations and comparing it to the GPS-derived digital elevation model (DEM) of the salar. Although it is unusual for an equipotential surface other than the geoid to be used as a geodetic reference, the difficulty of reducing gravity observations to the geoid through 4000 meters of topography warrant this step.

We also address the question of how water might control salar topography. Unlike typical sediments, salt moves almost entirely in aqueous solution. Dissolved salt is transported in overland and groundwater flows until it is precipitated by evaporation, with complicating effects due to changes in dissolution rates, saturation state, evaporation rate, and wind and Coriolis forcing. While rainwater, groundwater, and surface water all play a role on the salar, we focus on direct precipitation because it is a regular phenomenon and is clearly involved in halite dissolution and redeposition across the breadth of the salar. Our coupled overland-flow/salt-transport model illustrates how rain might shape the surface over decadal periods.

2. DATA

2.1 DEM of the salar de Uyuni

The best existing topographic data for the salar de Uyuni is the DEM generated from a 2002 kinematic GPS survey for the purpose of establishing a reference surface for satellite altimeter calibration and validation [*Borsa et al.*, 2008]. This GPS DEM is a 54 x 45 km uniform grid (Figure 2) whose coordinates are vertically referenced to the World Geodetic System 1984 (WGS84) ellipsoid and have an estimated vertical error of 2 cm root-mean-square (RMS) with respect to the true physical surface. DEM elevations range over 78 cm, from a low of 3696.87 m in the south to 3697.65 m in the northeast, with the general trend between these two extremes mimicking the slope of the long-wavelength geoid.

2.2 Gravity measurements at the salar de Uyuni

We obtained detailed gravity data for the salar de Uyuni from a compilation of regional observations described by Cady and Wise [1992]. The gravity measurements we use are from stations in the Yacimientos Petroliferos Fiscales Bolivianos (YPFB) portion of the dataset. From the YPFB data, we selected a subset of 10,894 points located within a 140 x 140 km bounding box centered on the salar (Figure 2), manually deleting 21 points whose free-air corrected gravity values varied more than 3 standard deviations from the mean of neighboring points.

The YPFB, which made these gravity measurements four decades ago as part of a oil and gas resources survey, is Bolivia's national oil company. Although it made the raw gravity data from this survey available, the YPFB did not release metadata or information about the methods used to obtain the measurements. Each record consists only of geographic latitude, longitude and elevation in an unspecified datum, and raw gravity reported to 0.01 mGal. While plotting gravity station locations onto a WGS84-referenced LANDSAT image, we noticed several hundred meters of horizontal offset with respect to physical features such as roads that the gravity survey

appears to follow. The direction and magnitude of this offset is consistent with a datum shift between WGS84 and the Provisional South American Datum 1956 for Bolivia (PRP-A) [*NIMA*, 1997]. We transformed gravity station latitude and longitude to WGS84 coordinates assuming the original data were in the PRP-A datum and observed that the offset with respect to LANDSAT features disappeared.

Mean gravity station elevation within the salar GPS survey area is 3653.55 m. This is 0.77 m lower than the mean WGS84/EGM96 geoidal height of the GPS DEM, which we obtained by adding to the DEM elevations the geoidal undulation (vertically referenced to the WGS84 ellipsoid) from Earth Gravitational Model 1996 [*Lemoine et al.*, 1998].

2.3 Low-resolution DEM of the Bolivian Altiplano

For the purpose of modeling terrain effects on gravity, we obtained the 90 meter resolution Shuttle Radar Topography Mission (SRTM) DEM for the region encompassing the salar de Uyuni. SRTM coordinates are also in the WGS84 datum, vertically referenced to the WGS84/EGM96 geoid. The SRTM DEM has a quoted horizontal accuracy of ±20 m and a vertical accuracy of ±10 m at the 90% confidence level over distances of 200 km [*Rabus et al.*, 2003]. Over the salar GPS survey area, the SRTM DEM gives a mean height of 3659.10 m, compared to 3654.32 m for the mean WGS84/EGM96 geoidal height of the GPS DEM. This indicates that the SRTM DEM is high by about 5 meters in the region, which is within the stated accuracy of the dataset.

2.4 Co-registering the Datasets

Based on the comparisons above, we shifted all SRTM elevations downwards by a uniform 4.78 m and all gravity station elevations upwards by 0.77 m to remove biases with respect to the GPS DEM. We then added WGS84/EGM96 geoidal heights (calculated at the full degree-360 model resolution) to the SRTM and gravity station elevations so that all elevations (GPS, SRTM,

and gravity) would be vertically referenced to the WGS84 ellipsoid. The only caveat is that gravity station elevations were likely obtained by spirit leveling, which would introduce a relative error between station elevations and the GPS DEM on the order of local undulations of the geoid. On the salar, the geoid is flat to within decimeters, so the resulting errors are negligible.

3. OBTAINING THE EQUIPOTENTIAL SURFACE AT THE SALAR DE UYUNI FROM GRAVITY OBSERVATIONS

3.1 Defining the Salar Reference Ellipsoid and Equipotential Surface

The study of Earth's equipotential surfaces has historically focused on determining the shape of the geoid, loosely defined as the equipotential surface of Earth's gravity field corresponding to mean sea level. The problem is traditionally posed in terms of defining the undulations of the geoid about the surface of a standard mean Earth reference ellipsoid that closely approximates Earth's mean shape and mass. Our aim is to describe an equipotential surface almost four kilometers above the geoid, an alternative problem whose theoretical development is similar to the canonical approach for the geoid as described in Heiskanen and Moritz [1967].

We follow convention by defining our equipotential surface of interest as the set of points in Earth-centered Cartesian space that satisfy the relationship $W(x, y, z) = W_0$, where W is the scalar geopotential field and W_0 is an appropriate constant geopotential value. Since we are trying to determine whether the topographic surface of the salar de Uyuni is an equipotential surface, a reasonable choice for W_0 is the approximate geopotential value associated with the center of the salar DEM. We use the EGM96 model to obtain $W_0 = 62601127.53$ m^2/s^2 at WGS84 ellipsoidal coordinates 20.21189S, 67.42253W, 3697.30 m. Although there is an infinite family of nearby

equipotential surfaces that could be used for this comparison, differences in shape between closely-spaced equipotential surfaces are negligible and can be ignored.

The reference ellipsoid is similarly defined as the level ellipsoid satisfying $U(x, y, z) = U_0$, where the gravity potential field U (the normal potential field) is considered to be generated by a homogenous interior mass distribution. In theory, any of the standard mean Earth ellipsoids could be used for the calculation of an equipotential surface at the elevation of the salar de Uyuni, but choosing an ellipsoid many kilometers below surface gravity observations complicates estimation of the Helmert gravity anomaly and can introduce large errors in the gravity reduction. We circumvent this problem by choosing a new reference ellipsoid that has the same Earth gravitational constant GM, rotation rate ω and flattening f as the WGS84 mean earth ellipsoid, but a semi-major axis (a = 6381835.7776 m) that causes the surface of the ellipsoid to pass through the coordinates used to calculate W_0 above. From Stokes' Theorem, the location of an axisymmetrically-distributed mass within an ellipsoid does not change the potential field at the ellipsoid boundary. This implies that the standard equations for normal potential and gravity on this new "salar ellipsoid" correspond to the upward-continued harmonic fields generated by the WGS84 ellipsoid, ensuring that the new reference potential approximates the geopotential at the salar elevation. Using WGS84 ellipsoid parameter values with the new semi-major axis from above, we calculate the normal potential U_0 in closed form [*Heiskanen and Moritz*, p.67] as 62600674.16 m^2/s^2.

3.2 Stokes' Formula

Our generalized approach takes the usual route of relating the equipotential surface undulations N to the gravity anomaly Δg via Stokes' formula. To incorporate our choice of an arbitrary reference ellipsoid and equipotential surface, we make two slight modification to the

standard calculation. First, we calculate the gravity anomaly Δg by subtracting normal gravity γ on the salar ellipsoid (rather than on the WGS84 ellipsoid) from observed gravity. Second, we use the generalized Bruns' formula [*Heiskanen and Moritz*, p. 100] to define the equipotential surface undulation, which includes a term to account for the fact that the geopotential value W_0 on our chosen equipotential surface is not the same as the normal potential U_0. The solution of Bruns' formula (in planar coordinates because of the limited extent of our gravity data) is Stokes' formula [*Schwarz et al.*, 1990]

$$N\left(x_P, y_P\right) = \frac{1}{2\pi\gamma} \iint_E \Delta g\left(x, y\right) S\left(x - x_P, y - y_P\right) dx dy \; + \; \frac{U_0 - W_0}{\gamma} \tag{1}$$

where γ is normal gravity averaged over the local domain E, and the Stokes' kernel S is given by

$$S\left(x - x_P, y - y_P\right) = \left[\left(x - x_P\right)^2 + \left(y - y_P\right)^2 \right]^{-1/2}. \tag{2}$$

When written in terms of the Fourier transform of (1) [*Sideris and Li*, 1993], Stokes' formula becomes

$$N\left(x, y\right) = \mathbf{F}^{-1}\left[\frac{1}{2\pi\gamma \left|\mathbf{k}\right|} \mathbf{F}\left[\Delta g\left(x, y\right) \right] \right] + \frac{U_0 - W_0}{\gamma} \tag{3}$$

where $\mathbf{k}$ the wavevector $<k_x, k_y>$ of coordinate wavenumbers corresponding to each Fourier component of $\mathbf{F}[\Delta g]$. The division of $\mathbf{F}[\Delta g]$ by the wavevector magnitude $|\mathbf{k}|$ attenuates the shortest wavelengths in the gravity field the most, which means that the equipotential surface N resembles a smoothed version of the gravity anomaly.

3.3 Calculating the Helmert Gravity Anomaly

While the Stokes' calculations in (1) and (3) assume that the gravity anomaly Δg is measured directly on the equipotential surface being estimated and that there is no mass above this surface,

this is rarely the case for actual gravity observations. Following recent convention, we employ Helmert's second condensation method [*Heiskanen and Moritz*, p. 145] to reduce observed gravity measurements to their corresponding values on the equipotential surface and to compensate for topographic mass, ignoring atmospheric mass because of the proximity of our measurements in distance and elevation. Using the Moritz-Pellinen (MP) approach [*Jekeli and Serpas*, 2003], the (Helmert) gravity anomaly is

$$\Delta g = g^{observed} + \delta g^{direct} + \delta g^{indirect} + \delta g^{FA} - \gamma \tag{4}$$

where adjustments to observed gravity ($g^{observed}$) are made to compensate for the direct topographic effect (δg^{direct}) of redistributing topographic mass to an infinitesimal layer on the equipotential surface, the secondary indirect effect ($\delta g^{indirect}$) to correct for the effect of the mass redistribution on potential, and the free-air reduction (δg^{FA}) to move the observation point from the topographic surface to the equipotential surface. Normal gravity γ from the salar reference ellipsoid is evaluated using the Somigliana formula [*Heiskanen and Moritz*, p. 70] at the location of each gravity measurement. For these calculations we project the latitude/longitude of the YPFB stations and SRTM data into Universal Transverse Mercator (UTM) coordinates and transform all elevations from heights above the WGS84 ellipsoid to heights above the salar ellipsoid.

We numerically evaluate the direct topographic effect at the location of each gravity measurement with topography from the SRTM DEM, using the standard formula

$$\delta g^{direct}\left(x_P, y_P\right) = \frac{G\rho}{2} \iint_E \left(h\left(x, y\right) - h_P\right)^2 S\left(x - x_P, y - y_P\right)^3 dxdy \tag{5}$$

where the subscript *P* indicates the coordinates of gravity observations, *h* is topographic elevation, *G* is the gravitational constant, ρ is rock density at the canonical value of 2670 kg/m^3

[*Hinze*, 2003], and $S(x, y)$ is the Stokes' kernel. Figure 3 shows the direct effect calculated for the entire salar de Uyuni region, with values ranging from 0.016 to 39 mGal and a mean of 1.4 mGal. As expected, higher values occur on or near rough topography, while on the salar itself the direct effect is close to zero.

The indirect effect is the vertical shift of the equipotential surface due to the geopotential change brought about by the topographic mass redistribution. Since the Helmert anomaly is evaluated on the equipotential surface, the effect of this shift on gravity must be considered. Because our choice of equipotential surface results in so little redistributed mass, the secondary indirect effect on gravity does not exceed 0.002 mGal in magnitude – a value smaller than the several approximation errors in the overall calculation. We therefore ignore this effect on the Helmert anomaly, setting $\delta g^{indirect}$ in (4) to zero.

The traditional way to downward-continue gravity anomalies from the topographic surface to the equipotential surface is via the free-air reduction [*Heiskanen and Moritz*, 1967, p.115], typically expressed as the first term of the Taylor expansion of normal gravity in height above the geoid

$$\delta g^{FA} \; ; \; -\frac{\partial \gamma}{\partial h} h \, . \qquad (6)$$

It is assumed in (6) that the intervening mass has been removed or redistributed and that the contribution of gravity from the non-normal (i.e. disturbing) potential field is ignored. The latter assumption can be problematic for high-elevation surveys such as ours, since errors due to ignoring the disturbing potential field are compounded as the height of the gravity measurements above the geoid increases. While it is possible to account for the disturbing potential by the downward continuation of actual gravity measurements via Poisson's integral, this approach

requires dense gravity observations over a large area and magnifies any errors or gaps in the measurements [*Bayoud and Sideris*, 2003].

We minimize the risks inherent in downward continuation by using a reference equipotential surface close to the gravity measurements (rather than the geoid, which is 4 km below) and estimating the free-air correction from

$$\delta g^{FA} \; ; \; -\left(g^{EGM96} - g_{h_o}^{EGM96} \right) \tag{7}$$

where g^{EGM96} is EGM96 model gravity at the measurement height and $g_{ho}{}^{EGM96}$ is model gravity at the equipotential surface height h_o corresponding to the potential value W_0. This is more accurate than using the normal gradient for the correction, since the EGM96 model also includes most of the long-wavelength curvature present in the actual gravity field. We note that on the salar, gravity measurements are made so close to the equipotential surface that the free-air reduction is effectively zero.

Finally, the redistribution of mass onto the equipotential surface results in an "indirect effect" on the geopotential that shifts the equipotential surface at any given point by some value δN. We calculated the indirect effect using the gravitational potential equations from the MP approach and determined that within the boundaries of the salar GPS survey the indirect effect was uniformly less than 1 mm and could therefore be ignored.

3.4 Remove-Restore Calculation

Calculating the free-air correction as we do in (7) makes it very easy to implement the standard "remove-restore" technique for minimizing error due to ignoring the long-wavelength gravity field in the locally-evaluated planar Stokes' formula. We remove long-wavelength gravity from the Helmert anomaly by subtracting tide-free EGM96 gravity values on the equipotential surface ($g_{ho}{}^{EGM96}$), ignoring the ~2 mm elevation slope over region due to the

permanent solid earth tide. EGM96 is a degree-360 spherical harmonic geopotential model, which means that it contains wavelengths down to approximately 110 km ($2\pi R_{earth}/360$). In the following discussion, we will use the term "long-wavelength" for wavelengths 110 km and longer, and "short-wavelength" for wavelengths less than 110 km.

Subtracting $g_{h_o}^{EGM96}$ cancels the corresponding term in the free-air calculation, resulting in the residual Helmert gravity anomaly equation

$$\Delta g^R = g^{observed} + \delta g^{direct} - g^{EGM96} - \gamma \tag{8}$$

where the indirect effect term has also been dropped. Substituting Δg^R for Δg allows us to generate the residual equipotential surface N^R via (3). The actual equipotential surface N is obtained from N^R by restoring the long-wavelength undulation from EGM96, as discussed below.

3.5 Fourier Expansion of the Helmert Gravity Anomaly and the Solution of Stokes' Formula

To evaluate Stokes' formula in (3) typically requires gridded values for the Helmert gravity anomaly, with the analytical Fourier transform recast as a discrete Fourier transform (DFT). Since most gravity surveys follow roads and other navigable terrain, use of the DFT requires resampling and interpolating gravity datasets that often contain large areas with no observations. This presents a considerable challenge for most gridding algorithms, since the autocorrelation information needed for accurate interpolation across large data gaps is difficult to assess from the survey data itself. In addition, the gravity field is not necessarily stationary over the survey region and is likely to be anisotropic, which means that its autocorrelation statistics may vary with location and azimuth.

To eliminate the need for gridding altogether, we adopt an alternative approach to the DFT whereby we model the short-wavelength gravity field via the least-squares fitting of harmonic basis functions to the residual Helmert gravity anomaly data. This approach is motivated by the use of finite harmonic series for trend analysis of potential data [*Bhattacharyya*, 1965; *Henderson and Cordell*, 1971; *James*, 1966] and closely follows the formal treatment given in Duijindam et al. [1999] for application to seismic signals.

Using the same Fourier expansion that appears in the DFT, we model the residual Helmert gravity anomalies from (8) as

$$\Delta g^R\left(x_i, y_i\right) = \sum_{a=-A}^{A} \sum_{b=-B}^{B} c\left(a,b\right) e^{2\pi i\left(x_i a / L_x + y_i b / L_y\right)} \tag{9}$$

where the exponentials are planar harmonic functions parameterized by their fundamental wavelengths L_x and L_y, and the $c(a,b)$ are complex expansion coefficients. L_x and L_y are the longest wavelengths in the fit, and we set both to 280 km to create an empty border around the 140 x 140 km data window. This allows all model wavelengths to freely adjust to their periodic extensions in the plane, mirroring the practice of tapering and zero padding in the DFT [*Henderson and Cordell*, 1971]. The parameters A and B determine the shortest wavelengths of the fit (i.e. L_x/A and L_y/B) and are chosen so that the resolution of the basis set is matched to the smallest significant wavelengths in the data. Because the spacing between north-south and east-west survey lines is quite variable, we take the model resolution to be identical in both coordinate directions, setting $A = B$.

Since (9) is linear in the coefficients $c(a,b)$, we represent it as the overdetermined system of equations

$$\Delta g^R = \mathbf{D}c\,, \tag{10}$$

where Δg^R is the N-vector of residual gravity anomaly observations, c is an M-vector of unknown coefficients and $\mathbf{D}$ is the $N \times M$ design matrix of basis vectors consisting of the harmonic functions evaluated at each point (x_i, y_i)

$$\mathbf{D} = \begin{pmatrix} e^{2\pi i\left(-x_1 A/L_x - y_1 B/L_y\right)} & \cdots & 1 & \cdots & e^{2\pi i\left(x_1 A/L_x + y_1 B/L_y\right)} \\ \vdots & & \vdots & & \vdots \\ e^{2\pi i\left(-x_N A/L_x - y_N B/L_y\right)} & \cdots & 1 & \cdots & e^{2\pi i\left(x_N A/L_x + y_N B/L_y\right)} \end{pmatrix}. \qquad (11)$$

With L set to 280 km, we obtained normal equation solutions of (10) for a range of $A = B$ values and examined the resulting models. While higher values of A and B inevitably result in better fits to the data, "dimpling" artifacts appear once the model resolution is higher than the spacing between survey lines. The highest-resolution model that does not exhibit dimpling between survey lines is formed by taking $A = B = 16$. This model has 1088 terms, a horizontal resolution of 17.5 km, a data misfit of 0.95 mGal RMS and almost no spatial correlation in its fit residuals. Unfortunately, it also exhibits large-amplitude fluctuations off the salar, where there is no data to constrain it (Figure 4a). This occurs because on an unevenly sampled domain such as ours, the inner products between the individual basis vectors comprising $\mathbf{D}$ are not necessarily zero, violating the orthogonality condition necessary for the stability of the solution. Although a solution is obtained, some linear combinations of basis vectors have negligible variance, allowing certain expansion coefficients to take on large values without impacting the goodness of fit. This is unacceptable for our application because the wavenumber division in Stokes' formula spreads out long-wavelength energy in the gravity anomaly, allowing model anomalies outside the data boundaries to contaminate the calculation of the equipotential surface inside them.

3.6 Stabilizing the Gravity Anomaly Expansion

We address the stability issue by constructing an orthonormal basis set from the basis vectors in **D** and then choosing a subset that allows a close fit to the data while minimizing the norm of the model coefficients – a technique often referred to as the method of empirical orthogonal functions. While previous gravity studies have used orthonormalized Legendre polynomials to model global gravity anomaly data [e.g., *Albertella et al.*, 1999; *Hwang*, 1993; *Pail et al.*, 2001], we use orthonormalized planar Fourier polynomials for the purpose of modeling regional gravity anomaly data. For our problem, we employ truncated singular value decomposition (TSVD) of the design matrix **D** [*Hansen et al.*, 1992; *Xu*, 1998], beginning with the standard singular value decomposition

$$\mathbf{D} = \mathbf{U}\Lambda\mathbf{V}^{\mathrm{T}} \tag{12}$$

where the columns of the $N \times M$ matrix **U** form an orthonormal basis $< u_1, \ldots, u_N >$ for the original basis vectors $< d_1, \ldots, d_N >$ in **D**, and $\mathbf{\Lambda}$ is an $N \times N$ diagonal matrix of singular values λ_i.

Using (12) we rewrite the expansion of the residual Helmert gravity anomaly data in (10) as

$$\Delta g^R = \mathbf{U}\Lambda\mathbf{V}^{\mathrm{T}} c \tag{13}$$

whose associated least-squares problem has the normal equation solution

$$c = \mathbf{V}\Lambda^{-1}\mathbf{U}^{\mathrm{T}}\Delta g^R \ . \tag{14}$$

Small singular values indicate orthonormal basis vectors u_i that are very nearly linearly dependent with other members of the basis set and thus will contribute least to the fit of Δg^R. TSVD techniques drop the k smallest-eigenvalue u_i by setting their inverse singular values in $\mathbf{\Lambda}^{-1}$

to zero. This damps model fluctuations without significantly affecting the fit to the data, giving us the new truncated solution

$$c_k = \mathbf{V}\Lambda_k^{-1}\mathbf{U}^{\mathrm{T}}\Delta g^R \tag{15}$$

where $\mathbf{\Lambda}_k^{-1}$ is the zeroed-coefficient version of $\mathbf{\Lambda}^{-1}$.

We employ the commonly-used "L-curve" technique to choose a cutoff value k simultaneously minimizes model size and model misfit, plotting the model norm $\|c\|$ against misfit $\|\Delta g - \mathbf{D}c\|$ for various k and specifying a truncation level that corresponds to the maximum curvature point of the graph [*Hansen et al.*, 1992]. Analyzing a representative plot for our data (Figure 5) we choose a truncation of $k = 610$ to minimize overall model variance. The 478-term truncated model calculated from (15) is much better behaved outside the data boundaries, at the acceptable cost of an increase in RMS misfit to 1.85 mGal (Figure 4b). The artifacts that remain are short-wavelength and therefore minimally impact the equipotential surface determination that we describe below.

3.7 Estimating the Equipotential Surface

Rewriting the Fourier Stokes' formula from (3) in terms of the harmonic expansion of the residual Helmert gravity anomaly, we obtain

$$N^R(x,y) = \frac{1}{2\pi\gamma}\sum_{a=-A}^{A}\sum_{b=-B}^{B} c(a,b)\frac{e^{2\pi i(xa/L_x + yb/L_y)}}{\sqrt{(a/L_x)^2 + (b/L_y)^2}} + \frac{U_0 - W_0}{\gamma} \tag{16}$$

where each expansion term has an associated wavenumber

$$\mathrm{k}(a,b) = |\mathbf{k}(a,b)| = \left[(a/L_x)^2 + (b/L_y)^2\right]^{-1/2}. \tag{17}$$

In matrix form the first term in (16) is expressed as

$$\mathbf{N}^R(x,y) = \frac{1}{2\pi\gamma}\mathbf{D}'(x,y)\mathbf{K}^{-1}c \qquad (18)$$

where $\mathbf{D}'(x, y)$ is a matrix of harmonic basis functions evaluated at the points where the equipotential surface undulation is sought (identical in construction to the design matrix **D**, but evaluated at different locations), and **K** is a diagonal matrix whose elements are the wavenumbers k(a, b). We handle the singularity at $k(0, 0) = 0$ by subtracting the mean value from Δg^R before fitting in (9) and removing the (0, 0) term from the fit.

Using the truncated model coefficients from (15), we calculate the short-wavelength equipotential surface model N^R shown in Figure 6. Aside from the scaling provided by normal gravity, the only difference between this model and the Helmert anomaly expansion in Figure 4b is smoothing due to the wavenumber division. The full equipotential surface N is obtained from

$$N = N^R + N^{EGM96} \qquad (19)$$

where the "restored" long-wavelength undulation N^{EGM96} is calculated from the EGM96 model using the salar reference ellipsoid to generate the normal field.

3.8 Error in the Equipotential Surface Estimation

The Stokes calculation for N^R specifically deals with short wavelengths of the gravity field, with longer wavelengths accounted for by the remove-restore method. We divide our discussion of error accordingly, beginning with the known errors in the EGM96 that impact the accuracy of the remove-restore components g^{EGM96} and N^{EGM96}. EGM96 error is quite low at longer wavelengths, but increases considerably at shorter wavelengths. Cumulative error grows from 14.5% of the RMS signal strength at degree 120 (330 km wavelength) to 35.4% at degree 360 (110 km wavelength) [*Lemoine et al.*, 1998]. Since we can expect the largest errors in the YPFB survey to be at the longest wavelengths in the data [*Heck*, 1990], survey errors will combine with

errors in g^{EGM96} to greatly limit the accuracy of our Helmert gravity anomaly model at wavelengths in the range of 100~200 km. Fortunately, over the relatively small area of the salar where we compare DEM topography and the YPFB-derived equipotential surface, these long-wavelength errors will manifest themselves primarily as a residual planar trend which can easily be removed. N^{EGM96} will also contain errors at these wavelengths, similarly manifested as a planar trend across the comparison region.

As for the Stokes' calculation, choosing an equipotential reference surface near the mean elevation of the gravity stations in the YPFB survey dramatically reduces the short-wavelength errors associated with estimating the Helmert gravity anomaly from the raw gravity data. We were unable to identify error sources that would contribute more than about 1 mGal average error in the calculations for direct/indirect effects or the free-air reduction. Furthermore, on the salar itself, the lack of topography and the fact that gravity measurements are made within a few decimeters of the equipotential surface means that there is minimal gravity reduction required, with correspondingly negligible errors.

What this means from the standpoint of the error in N^R at different component wavelengths can be determined directly from (18). For the 17.5 km minimum wavelength in the model, a 1 mGal error in the gravity anomaly expansion coefficient yields a 2 mm error in N^R. At the 280 km maximum wavelength, the error is approximately 3 cm. These two extremes are bounds on the Helmert anomaly expansion error. The 1.85 mGal RMS misfit between our truncated expansion model and the Helmert anomaly data might appear to be a significant error source, but since it is entirely due to structure in the gravity field at wavelengths shorter than those in our expansion, the corresponding omission error in N^R is likely to be on the order of millimeters.

A potential shortcoming of our gravity anomaly model is that it incorporates no direct measurements of the gravity field within the data gaps of the YPFB survey. To estimate the impact of the missing data, we simulated its effect on the estimation of N^R using a synthetic gravity anomaly field with a band-limited red spectrum (spectral index of 1, wavelengths between 17.5 km and 280 km) and a magnitude equivalent to that of the measured anomalies around the salar. We sampled this anomaly field at the station locations in the YPFB survey, substituted these values for our original Helmert anomalies, and calculated the corresponding equipotential surface using the same algorithm we used for actual YPFB data. Comparing this surface with the one calculated from the full synthetic dataset, we find uniform vertical biases of up to 4 cm over the area of our salar GPS survey. Such biases are due to the magnification of long-wavelength error through wavenumber division, but since they do not affect our comparison of relative shape of salar topography compared to the equipotential surface, they are not of concern here. More importantly, our results also show that the gravity data gaps have a negligible effect on the shape of the equipotential surface where it overlaps with the salar DEM.

4. RESULTS

To test our hypothesis that topography on the salar de Uyuni describes an equipotential surface of Earth's gravity field, we compare the equipotential surface estimated above with topography from the GPS-derived DEM of the salar. Because of long-wavelength error introduced by the EGM96 model, we cannot do this comparison directly. Instead, we proceed stepwise with topography from the salar DEM (Figure 7a). DEM elevations are referenced to the salar reference ellipsoid and have a 12.9 cm standard deviation and a range of 70 cm (see Table 1).

Figure 7b shows the EGM96 equipotential surface *A* that passes through the centerpoint of the salar DEM. This long-wavelength equipotential surface correlates well with the long-wavelength topography: both rise to the northeast and show similar broad-scale curvature. Subtracting *A* from the DEM yields a topographic residual (*DEM minus A*, Figure 8a) whose standard deviation is 9.4 cm and range is 42 cm.

DEM minus A contains the cumulative error present in all degrees of the EGM96 model. As discussed in Section 3.8, we assume that the error over the 45 × 54 km domain of comparison should manifest itself primarily as a residual planar trend in the data. We estimate this trend by a least-squares planar fit to *DEM minus A*, obtaining plane *B* (Figure 8b). Removing this plane gives us detrended residual topography (*DEM minus A+B*, Figure 9a) with a standard deviation of 7.8 cm, whose dominant feature is a broad NE-striking ridge flanked by depressions to the NW and SE.

The short-wavelength equipotential surface calculated from the YPFB gravity data is also contaminated by long-wavelength EGM96 error due to the fact that we remove EGM96 gravity when calculating the residual Helmert anomaly. We remove the best-fitting plane from the portion of the equipotential surface within the DEM domain to obtain the detrended equipotential surface *C* (Figure 9b).

Comparing the detrended residual topography with the detrended equipotential surface (Figures 9a and 9b) shows that despite differences in short-wavelength details, these surfaces are a close match. Differencing the two gives a residual surface (*DEM minus A+B+C*, Figure 10a) with a standard deviation of only 3.4 cm. What is striking about this representation of salar topography is how little of the original topographic variance remains. Referencing the DEM to the salar equipotential surface (which is what the steps leading to *DEM minus A+B+C* entails)

explains 93% of topographic variance – a result that one might expect for a body of water, but not for the solid earth.

A potential explanation for the remaining topographic variance is that it is simply error in the DEM or in the derived equipotential surface. We are fortunate to have an independent estimate of geoid-referenced topography obtained via optical absorption measurements of the flooded salar from MISR, the Multiangle Imaging SpectroRadiometer [*Bills et al.*, 2007] (Figure 10b). Bills et al. (2007) specifically measure water depth, but since the water surface is also nominally an equipotential surface, their method gives height with respect to the salar equipotential surface. Despite possible error in the MISR measurement due to wind forcing, the two estimates of residual topography are remarkably similar. The standard deviation of their difference is 2.3 cm, due to both the higher MISR resolution as well as unidentified longer-wavelength errors. Since the errors in the two estimates should be uncorrelated, 2.3 cm is an upper bound on their combined error (and thus on their individual errors as well).

The final product of our gravity modeling is the composite equipotential surface derived from the sum of the EGM96 equipotential surface *A*, the plane *B*, and the short-wavelength equipotential surface *C* (Figure 11). This is our estimate of the shape to which a body of water in the salar basin would conform under the influence of gravity alone. In the next section we introduce a process model that provides a possible explanation of why this shape closely matches the topography of the actual salar surface.

5. DISCUSSION

The salar de Uyuni is one of only a few places on Earth where the surface of a massive halite deposit is in regular contact with an ephemeral shallow-water lake. In such an environment, halite forms a hard, cemented crust which cannot be directly transported by wind and which

remains hard even when the surface is wet. When the salar floods, salt enters the water column via chemical dissolution at the salt/water interface rather than by entrainment due to the mechanical action of moving water. Water movement is relevant to the speed of salt dissolution, but only because it impacts the speed of vertical mixing. On the deposition side, halite is redeposited on the surface when it precipitates due to evaporation of saturated brine. While there is no relationship between current velocity and deposition rate as in the case with sediment transport, precipitated halite crystals can form "rafts" on the water surface that are susceptible to wind action.

If transport in solution is indeed the mechanism by which halite is moved about the surface, then answering the question of why the salar surface should closely approximate the shape of the gravitational equipotential ultimately depends on understanding the chemical interaction between water and salt, and the forces which physically move water around the surface. This question is not addressed in the literature on the formation and evolution of shallow-water halite deposits. Most studies of halite surfaces [e.g., *Lowenstein and Hardie*, 1985; *Schreiber and El Tabakh*, 2000] focus on interpreting the sub-meter-scale structure of the salt crust formed in the basins of ephemeral lakes. While these studies are relevant to explaining the smoothness of halite crusts under conditions of repeated flooding, they do not address the overall shape of the surface.

LANDSAT images from the past two decades confirm that the salar de Uyuni undergoes an annual cycle of flooding and desiccation, which provides an ideal aqueous environment for the dissolution, transport and redeposition of halite. The depth of inundation is quite variable from year to year, with the surface remaining nearly dry in some years and completely flooded for several months in others. What is not clear from the imagery is the source of the water on the salar. Water can be delivered to the salar as rain, surface runoff from the surrounding catchment,

or groundwater flow – each of which has different implications for the redistribution of salt. We focus here on the effects of rain because it is easily modeled and because we have the necessary observational data. Surface runoff and groundwater flow should generate a similar pattern of salt transport toward areas that are topographically depressed, with subtle differences that we will discuss later.

5.1 Salt Transport by Rainwater

Rain dissolves salt over the entire salar and generally carries salt from high areas to low via gravity-driven overland flow. We estimate average annual precipitation in the salar de Uyuni basin to be 24 ± 17 cm from rain gauge records at Salinas de Garci-Mendoza (just north of the salar) in the years between 1950 and 1980. Overlapping data from the still-operating Oruro station located 200 km further north shows a similar annual rainfall of 28 ± 11 cm. Most of this precipitation occurs during the summer rainy season between December and March and appears from recent daily records at Oruro to be the result of numerous rainfall events during these months rather than a few intense storms. Evaporation rates are not available for the salar itself, but existing studies suggest that evaporation from exposed brine in semi-arid climates ranges between 2.0 and 2.5 mm/day when averaged over the entire year [e.g., *Menking et al.*, 2000; *Tyler et al.*, 1997]. This rate varies temporally due to changes in wind, temperature and radiation flux. Where the evaporating brine layer is deeper than several centimeters and winds are calm, a floating crust of surface-nucleated halite "hoppers" can form, with an observed tenfold reduction in the evaporation rate [*Tyler et al.*, 1997]. Because sequential LANDSAT images of the salar often show many cm of water evaporating over periods of several weeks, we believe it unlikely that a hopper crust is typically present. A possible explanation is that floating salt accumulations are constantly broken up by wave action from persistent winds blowing across the long fetch of the salar.

Once on the surface, rainwater becomes quickly saturated due to the high dissolution rate of halite. If we take the Na^+ and Cl^- ratio to be parity, which is very close to the case on the salar [*Risacher and Fritz*, 2000], then we can express the rate of dissolution r as [*Alkattan et al.*, 1997]

$$r = k\left(1 - c/c_{sat}\right) \tag{20}$$

where c is the bulk solution concentration, c_{sat} is the saturation concentration and k is an empirically-determined rate constant. Simon [1981] finds k to be 5.5×10^{-6} m/s at 20°C and shows a weak linear trend in k with temperature of about 2% per °C. The corresponding value of c_{sat} at 20°C is 5416 mol/m^3 [*Kaufman*, 1960]. We make a rough estimate of time to saturation for fresh water of a given depth by integrating (20) (ignoring volumetric changes due to solution concentration) and applying the appropriate boundary conditions, assuming that rainfall impact and wind are sufficient to thoroughly mix the shallow water column (Appendix A). Our calculation shows that for depths ≤2 cm, fresh water becomes 95% saturated in under 4 hours (Figure 12). We will show in Appendix B that overland flow velocity for such depths is no more than about several hundred meters per day on the salar, which means that precipitated water is likely to be saturated before it moves even 100 meters downslope.

Because halite dissolution is so quick, it is not a limiting factor in salt transport due to precipitation. Transport is instead governed by interaction between the flow and evaporation of saturated rainwater as it moves across the surface of the salar. To model this rainwater-mediated salt transport, we developed a simple one-dimensional model and applied it to a topography transect across the salar DEM. The key aspects of this model are:

1.) Rain falls uniformly across the salar surface.

2.) The entire daily rainfall total is delivered once per day to mimic the late-afternoon peak

in thunderstorm activity that is responsible for most summer rainfall [*Garreaud*, 1999].

3.) When rainfall occurs, salt goes into solution up to the saturation limit and the height of the salar surface is correspondingly reduced by a factor of 0.147 of the rainfall depth. We base this ratio on the 2.16 g/cm^3 density of halite, its molecular weight of 58.4 g/mol and a saturation concentration of 0.00542 mol/cm^3 at 20°C.

4.) Saturation of precipitated water with halite is instantaneous.

5.) Water flows due to gravity forcing only, with no effects due to winds or tides. Since gravity flow is driven by differences in fluid height about the local equipotential surface, the topographic input to the model is referenced to the salar equipotential surface rather than to the WGS84 ellipsoid.

6.) Flow on the salar is considered to be laminar, as it is characterized by Reynolds' numbers of less than 100 (we assume a nominal water depth *a* of 1 cm, water velocity *u* of 1 cm/s, and kinematic viscosity of 1.61×10^{-6} m^2/s). We model this flow using a form of the Navier-Stokes equations relevant to a one-dimensional laminar flow regime (Appendix B).

7.) Evaporation is spatially and temporally uniform, with no provisions for wind, radiation or other effects on the evaporation rate.

8.) Since surface water is considered to be saturated at all times, evaporation is accompanied by the redeposition of salt in accordance with the 0.147 factor cited above.

We use the July, 2002 ~ June, 2003 rainfall record from Oruro to provide the rainfall input to

our model (Figure 13). The precipitation total during this period is 29.5 cm, which is 23% higher than the estimated average salar de Uyuni rainfall, but well within the one-sigma limits of rainfall variability. The topographic input to our model is the transect in Figure 14 across *DEM minus A+B+C*. Although we could have used simulated topography, we were interested to see how long it would take to flatten the observed topographic residual with respect to the salar equipotential surface.

To illustrate the overland flow produced by our model with the topographic profile above, we show in Figure 15 a sequence depicting the flow and evaporation of surface water from a single 2-centimeter rainfall event. Surface water starts off as a uniform layer (Figure 15a), which immediately begins to move downslope and pond in low-lying areas (Figure 15b). Evaporation gradually lowers the level of ponded water (Figure 15c) until the surface is again dry. Although we do not show salt transport here, salt is dissolved in the initial rainfall and is carried by the surface water flow. It preferentially precipitates in the low areas where most evaporation occurs.

We run the full flow/transport model for ten years, using the same rainfall input each year for the purpose of consistency. Figure 16a shows the successive evolution of the surface, starting from the "high-relief" original transect and progressing to the nearly-flat profile at the end of year 10. Since the initial topography is referenced to the salar equipotential surface, the free water surface in our model is horizontal. The model profiles therefore evolve toward the equipotential surface under conditions of natural precipitation, which agrees with our observation that the salar surface very closely approximates the shape of the gravitational equipotential. Surface evolution slows considerably in later years as the topographic slope drops almost everywhere to less than 1×10^{-6} and flow velocity decreases accordingly. Slower flow leads to

slower salt transport because the salt is not transported as far before it is redeposited onto the surface via evaporation.

Higher evaporation rates slow salt transport as well. The direct effect of increased evaporation is to precipitate salt higher on the slopes. But there is also an indirect effect on salt transport due to the decrease in water depth from evaporation: flow velocity is proportional to the square of depth, which means that salt transport is slowed considerably as depths get small. We test the impact of a higher evaporation rate on our model by increasing the evaporation rate by 25%, to 2.5 mm/day. The result is the set of profiles in Figure 16b, which show a relative slowdown in the profile evolution once the high initial slopes disappear. This suggests that in a high-evaporation/low-slope regime, large rain events do most of the salt transport, since it is only then that the flow velocity is high enough to overcome the quick evaporation.

5.2 Salt Transport by Surface Runoff

Based on the low level of dissolved salts found in the inflow from the Rio Grande at the southeast corner of the salar [*Rettig et al.*, 1980], we believe that surface runoff onto the salar is mostly fresh water which dissolves salt near the salar perimeter before flowing out onto the surface. The surface dissolution of runoff can be seen as shallow water-filled "peripheral moats" (to use the phrase from Comstock and Bills [2004]), which are the darker areas around the edges of the salar in Figure 11. Even if the runoff does not completely mix with the denser brines in the moats, it should become saturated quickly as it moves onto the salar. This provides a mechanism for moving salt from the edges of the salar toward the center. Assuming that the volume of water involved is fairly large, runoff events will result in quick flow across the salar. Evaporation will precipitate a layer of salt across the salar proportional to water depth. Deeper areas will be preferentially filled at the expense of shallower areas, with a qualitative effect similar to that of salt transport due to rainwater flow.

We do not attempt to model the effects of runoff for two reasons. First, it is unclear how often significant amounts of runoff reach the salar, let alone what the volume of runoff actually is. In most years, the amount of surface water apparent in satellite images of the salar can be entirely explained by direct precipitation alone. Second, even when inundation does occur, we do not know how runoff is distributed around the salar. It matters from the modeling standpoint whether water is delivered primarily by the three or four streams emptying into the salar or whether it just runs off directly from the surrounding catchment.

5.3 Salt Transport by Groundwater Flow

Groundwater moving into the salar de Uyuni basin from rainfall in the surrounding drainage area is likely to be a significant source of fresh water into the salar system. Since there are no comprehensive studies of groundwater movement in the area, we do not know how groundwater behaves in the subsurface. Our basic assumption, however, is that groundwater saturates underground due to contact with brine and solid halite and therefore does not dissolve halite at the surface.

On the deposition side of the equation, however, there is evidence that groundwater is important. Drilling pits dug into the salar have been observed to fill with salt in a span of two years (Bruce Bills, personal communication). Since the water table remains close to the salar surface throughout the year, these pits are always filled with brine. The evaporation rate from these pits is likely to be very high, both because the vapor-pressure gradient above an open-water surface is large and because the albedo of brine is much lower than that of salt. Evaporation will precipitate halite and drive a steady flow of brine into the pit through the subsurface. Over time, the pit will fill with salt. This may be a mechanism by which the salar provides a return flow of salt to the peripheral moats, since these are observed to be filled long after the rest of the surface

is completely dry. This mechanism should also serve to fill low-lying areas of the salar when the water table is near the mean surface level.

6. CONCLUSIONS

Although our discussion and analysis of salt transport on the salar is incomplete, we provide evidence that water-mediated salt transport in all of its forms tends to push the salar surface toward an equilibrium shape that approximates the mean free surface of standing water on the salar. This accords with our observation that salar topography closely approximates the gravitational equipotential surface to which the free water surface conforms in the absence of tides and wind. The fact that there remains residual topography on the salar despite the constant leveling action of water suggests that topography is being actively maintained. Indeed, archived satellite images of the flooded salar show that features on the surface are stable for many decades, indicating a long-term dynamic equilibrium between generative and erosive forces on the salar.

We can guess at the nature of this topography-generating process, but its rigorous identification is an obvious direction for future work. The kilometer-scale wavelengths of the residual topography argues against the direct effect of moving water, simply because the surface water layer is never thick enough to support wavelengths longer than about a meter. An emergent property of an unknown dynamic system that involves water flow cannot be ruled out, however. Atmospheric waves are approximately the correct wavelength, but the pressure differential between peaks and troughs may be too small to affect the surface without some kind of positive feedback mechanism amplifying the signal. There is also the possibility of some subsurface force (circulating groundwater, mud diapirism in deep sedimentary layers, etc.) pushing the surface upward from below, although we have no evidence for this.

Simple field measurements to narrow the possibilities would focus on characterizing air and water flow across the salar. An array of pressure gauges deployed to several locations across the salar during the winter peak in east-west winds could determine the length scales of atmospheric waves in the region and might confirm whether known surface features correlate with stable or at least recurring atmospheric features. Arrays of water pressure gauges deployed for longer periods could help to establish the correlation between rainfall and surface water depth and would help determine the speed and variability of wind-driven currents on the salar. Even if these measurements were not conclusive by themselves, they could serve as inputs into a more complicated water flow model that might exhibit much more complex behavior than we have been able to simulate. Whatever the nature of this future work, we expect that it is only the beginning of a long effort toward understanding the geomorphology of this very unusual place.

APPENDIX A. SATURATION TIME FOR WELL-MIXED SODIUM CHLORIDE SOLUTIONS OF VARYING DEPTH

To estimate the time to reach a certain level of saturation for water overlying a smooth halite surface, we begin with the dissolution rate equation (20):

$$r = k\left(1 - c/c_{sat}\right) \tag{21}$$

where c and c_{sat} are the concentrations of NaCl (mol/m^3) in the bulk solution and at saturation, k is the rate constant for an infinitely dilute solution (m/s), and we assume that the water column is well-mixed. The units of r indicate a flux of salt dS per unit area per second, giving us

$$r = \frac{dS}{dt} \text{ per unit area.} \tag{22}$$

Since the bulk concentration in a well-mixed column of water is just total salt content divided by volume, for unit area and water depth a, we have

$$c = \frac{S}{a} \tag{23}$$

and

$$\frac{dc}{dt} = \frac{1}{a}\frac{dS}{dt}. \tag{24}$$

Because we are only concerned with a rough estimate of time to saturation, we ignore the fact that the volume of an aqueous NaCl solution expands by 13% as its concentration increases from zero to saturation (viz. a 26% NaCl solution by mass has a density of 1.1972 g/cm [*Lide*, 2007]). Inserting (24) into (21) gives an approximate equation for the change of concentration with time

$$\frac{dc}{dt} = \frac{k}{a}\left(1 - c/c_{sat}\right) \tag{25}$$

which we can integrate as

$$\int \frac{1}{1 - c/c_{sat}} dc = \int \frac{k}{a} dt \tag{26}$$

to get the expression

$$c = c_{sat} - Ce^{-kt/a}\,. \tag{27}$$

Since $c = 0$ at $t = 0$, the constant C is evaluated as c_{sat}, giving us the complete equation for the concentration of NaCl with time for fixed water depth a:

$$c = c_{sat}\left(1 - e^{-kt/a}\right). \tag{28}$$

We graph percentage saturation (c/c_{sat}) for a = 0.01 m, 0.02 m, 0.05 m and 0.10 m in Figure 13.

APPENDIX B. THE NAVIER-STOKES EQUATIONS FOR ONE-DIMENSIONAL OVERLAND FLOW

The Navier-Stokes equations for one-dimensional overland flow are a simplification of the two-dimensional Navier-Stokes overland flow equations, which in turn are derived from the full three-dimensional formulation by assuming a small vertical scale relative to horizontal and integrating over water depth. We use Vreugdenhil's [1994, pp.23-24] derivation of the 2-D mass conservation equation

$$\frac{\partial a}{\partial t} + \frac{\partial au}{\partial x} + \frac{\partial av}{\partial y} = q \tag{29}$$

and momentum conservation equations

$$\frac{\partial au}{\partial t} + \frac{\partial au^2}{\partial x} + \frac{\partial auv}{\partial y} - fav + ga\frac{\partial h}{\partial x} + \frac{ga^2}{\rho_0}\frac{\partial \rho}{\partial x} + \frac{\tau_{bx}}{\rho_0} - \frac{\partial aT_{xx}}{\partial x} - \frac{\partial aT_{xy}}{\partial y} = F_x \tag{30}$$

$$\frac{\partial av}{\partial t} + \frac{\partial av^2}{\partial y} + \frac{\partial auv}{\partial x} + fau + ga\frac{\partial h}{\partial y} + \frac{ga^2}{\rho_0}\frac{\partial \rho}{\partial y} + \frac{\tau_{by}}{\rho_0} - \frac{\partial aT_{yy}}{\partial y} - \frac{\partial aT_{xy}}{\partial x} = F_y \tag{31}$$

where x and y are the two horizontal coordinate directions, u and v are depth-averaged x and y velocities, a is water depth, q is water flux (i.e., rainfall, evaporation), g is the acceleration of gravity, h is the height of the water surface above the equipotential surface, ρ_0 is average water density, ρ is actual water density, τ_b is vertical bed stress given a no-slip bottom boundary condition, T is the sum of lateral stresses due to friction and advection, F is forcing due to wind, tides, etc., and f is the Coriolis parameter $2\omega\sin\theta$ with earth rotation rate ω and geographic latitude θ. We note that multiplying (30) and (31) by the average density ρ_0 restores their units to that of momentum (kg·m/s).

We simplify the equations for momentum conservation by using the standard assumptions of constant density and small lateral shear compared to vertical shear [e.g., *Esteves et al.*, 2000;

Fiedler and Ramirez, 2000; *Zhang and Cundy*, 1989]. We also follow the usual convention of ignoring the forcing terms F. This gives us

$$\frac{\partial au}{\partial t} + \frac{\partial au^2}{\partial x} + \frac{\partial auv}{\partial y} - fav + ga\frac{\partial h}{\partial x} + \frac{\tau_{bx}}{\rho_0} = 0 \tag{32}$$

$$\frac{\partial av}{\partial t} + \frac{\partial av^2}{\partial y} + \frac{\partial auv}{\partial x} + fau + ga\frac{\partial h}{\partial y} + \frac{\tau_{by}}{\rho_0} = 0\,. \tag{33}$$

Coriolis effects cannot be ignored in two-dimensional flow on the salar. If we calculate the Rossby number (e.g., the ratio of inertial to Coriolis forces) for average horizontal flow velocity u = 0.01 m/sec, length scale L = 10000 m and Coriolis parameter $f = 5\text{x}10^{-5}$, we obtain $Ro = u/fL$ = 0.02, which is significantly less than 1 and indicative of strong Coriolis forcing.

Focusing on flow in the x-direction only, we arrive at the one-dimensional dynamic-wave equations for shallow overland flow

$$\frac{\partial a}{\partial t} + \frac{\partial au}{\partial x} = q \ \text{(mass conservation)} \tag{34}$$

$$\frac{\partial au}{\partial t} + \frac{\partial au^2}{\partial x} + ga\frac{\partial h}{\partial x} + \frac{\tau_{bx}}{\rho_0} = 0 \ \text{(momentum conservation).} \tag{35}$$

where we note that the Coriolis term has dropped out. The first two terms of (35) are essentially the material derivative of momentum and represent the change in momentum as viewed from a fixed point in space. These are usually referred to as the inertial terms. The third term is the pressure force due to differential water surface height above the reference equipotential surface and is the sole driving force in these equations.

The fourth term in (35) is the density-normalized shear stress due to the no-slip condition at the bottom boundary of the water column. For a laminar flow regime such as exists on the salar de Uyuni, the appropriate form for τ_{bx} is [*Katz et al.*, 1995; *Zhang and Cundy*, 1989]

$$\tau_{bx} = \rho_0 \frac{K_0 v u}{8a} \quad (36)$$

where v is now kinematic viscosity and K_0 is the Darcy-Weisbach surface roughness parameter.

Examination of the Froude number (e.g., the ratio of inertial to pressure terms) indicates that the inertial terms in (35) are relatively small. We obtain $Fr = u^2/(ga) = 0.001$ using $u = 0.01$ m/s and $a = 0.01$ m. Such a small Froude number justifies using the diffusive wave approximation, whereby the inertial terms in the momentum equation are ignored for the sake of numerical stability [e.g., *Di Giammarco et al.*, 1996; *Ponce et al.*, 1978]. Using this approximation and incorporating (36), we obtain the simplified equations

$$\frac{\partial a}{\partial t} + \frac{\partial au}{\partial x} = q \text{ (mass conservation)} \quad (37)$$

$$ga\frac{\partial h}{\partial x} + \frac{K_0 v u}{8a} = 0 \text{ (momentum conservation).} \quad (38)$$

Rearranging (38) gives the flow velocity directly as

$$u = -\frac{8ga^2}{K_0 v}\frac{\partial h}{\partial x} \quad (39)$$

where we take $g = 9.7864$ m/s^2, $v = 1.61\text{x}10^{-6}$ m^2/s and $K_0 = 24$ for smooth laminar flow [*Katz et al.*, 1995]. For slopes of ~$1\text{x}10^{-5}$, which is a good average value for the salar, (39) predicts velocities in the range of 0.002~0.008 m/s for water depths of 1~2 cm. This is about 200~700 m/day, which is slow enough to ensure that precipitated water completely saturates before it has a chance to flow very far.

We implement closed boundaries in our model by setting outward velocities at the ends of the topographic transect to zero, and we take our initial flow and water depth to be zero. Together with these boundary conditions, (37) and (39) form a system of non-linear partial

differential equations whose solution must be found numerically. To prevent the calculation from becoming unstable, we impose a minimum depth of 1 mm in every model cell, below which flow out of the cell is stopped. This negligibly affects the accuracy of the salt transport for which the flow model is used.

We employ the widely-used second-order explicit MacCormack computational scheme to solve our diffusive-wave flow system [e.g., *Esteves et al.*, 2000; *MacCormack*, 1971]. Although this scheme is typically used for the full dynamic-wave equations, it is excellent at preventing oscillation in our simpler model as well. As applied to (37) and (39), the MacCormack scheme involves a predictor step

$$\bar{a}_x^{t+\Delta t} = a_x^t + q - \frac{(au)_{x+\Delta x}^t - (au)_x^t}{\Delta x} \tag{40}$$

$$\bar{u}_x^{t+\Delta t} = -\frac{8g\left(a_x^t\right)^2}{K_0 v}\frac{(a+z)_{x+\Delta x}^t - (a+z)_x^t}{\Delta x} \tag{41}$$

and a combined corrector/averaging step which incorporates the predicted depth and velocity

$$a_x^{t+\Delta t} = a_x^t + q - \frac{\Delta t}{2\Delta x}\left[\left((au)_{x+\Delta x}^t - (au)_x^t\right) + \left((\bar{a}\,\bar{u})_x^{t+\Delta t} - (\bar{a}\,\bar{u})_{x-\Delta x}^{t+\Delta t}\right)\right] \tag{42}$$

$$u_x^{t+\Delta t} = -\frac{8g\Delta t}{K_0 v 2\Delta x}\left[\begin{array}{l}\left(a_x^t\right)^2\left((a+z)_{x+\Delta x}^t - (a+z)_x^t\right) + \\ \left(\bar{a}_x^{t+\Delta t}\right)^2\left(\left(\bar{a}_x^{t+\Delta t} + z_x^t\right) - \left(\bar{a}_{x-\Delta x}^{t+\Delta t} + z_{x-\Delta x}^t\right)\right)\end{array}\right]. \tag{43}$$

In these equations, subscripts refer to spatial indexing, superscripts refer to temporal indexing, and z is height of the bottom boundary above the reference equipotential surface. Notice that forward differences are used in the predictor step and backward differences in the corrector step. We follow Esteves et al. (2000) in switching to backward/forward differences every other timestep in order to remove directional bias in the calculation.

We choose the topographic grid spacing Δx to be 100 m, which gives sufficient spatial resolution for the low-relief topography on the salar. We do not optimize Δt using the Courant stability condition as is typically done, but instead choose a timestep of 5 seconds because it is the largest time step that empirically proves to yield stable solutions. With these values of Δx and Δt, one year of model time requires about 15 minutes of real-time processing using a fast workstation.

ACKNOWLEDGEMENTS

We thank NASA's ICESat Mission for its support of this work. This research was funded through NASA contract NAS5-99006 to ICESat Team Member J-B. Minster.

REFERENCES

Albertella, A., et al. (1999), Band-limited functions on a bounded spherical domain: the Slepian problem on the sphere, *Journal of Geodesy*, *73*(9), 436-447.

Alkattan, M., et al. (1997), Experimental studies of halite dissolution kinetics, 1 The effect of saturation state and the presence of trace metals, *Chemical Geology*, *137*(3-4), 201-219.

Bayoud, F. A., and M. G. Sideris (2003), Two different methodologies for geoid determination from ground and airborne gravity data, *Geophysical Journal International*, *155*(3), 914-922.

Bhattacharyya, B. K. (1965), Two-dimensional harmonic analysis as a tool for magnetic interpretation, *Geophysics*, *30*(5), 829-857.

Bills, B. G., et al. (1994), Hydro-isostatic deflection and tectonic tilting in the central Andes: Initial results of a GPS survey of Lake Minchin shorelines, *Geophysical Research Letters*, *21*(4), 293-296.

Bills, B. G., et al. (2007), MISR-based passive optical bathymetry from orbit with few-cm level of accuracy on the salar de Uyuni, Bolivia, *Remote Sensing of Environment*, *107*(1-2), 240-255.

Borsa, A. A., et al. (2008), Topography of the salar de Uyuni, Bolivia from kinematic GPS, *Geophysics Journal International*, *172*(1), 31-40.

Cady, J. W., and R. A. Wise (1992), Gravity and magnetic studies, in Geology and Mineral Resources of the Altiplano and Cordillera Occidental, Bolivia, in *U.S. Geological Survey Bulletin*, edited by USGS, pp. 56-62.

Comstock, R. L., and B. G. Bills (2004), Topography of the flattest surface on Earth: using ICESat, GPS and MISR to measure salt surface morphology on salar de Uyuni, Bolivia, *Eos, Transactions, American Geophysical Union, Fall Meeting Supplement*, *85*(47).

Di Giammarco, P., et al. (1996), A conservative finite elements approach to overland flow: the control volume finite element formulation, *Journal of Hydrology*, *175*, 1267-1291.

Duijindam, A. J. W., et al. (1999), Reconstruction of band-limited signals, irregularly sampled along one spatial direction, *Geophysics*, *64*(2), 524-538.

Esteves, M., et al. (2000), Overland flow and infiltration modelling for small plots during unsteady rain: numerical results versus observed values, *Journal of Hydrology*, *228*(3), 265-282.

Fiedler, F. R., and J. A. Ramirez (2000), A numerical method for simulating discontinous shallow flow over an infiltrating surface, *International Journal for Numerical Methods in Fluids*, *32*(2), 219-239.

Fricker, H. A., et al. (2005), Assessment of ICESat performance at the salar de Uyuni, Bolivia, *Geophysical Research Letters*, *32*(21), L21S06.

1 Garreaud, R. D. (1999), Multiscale analysis of the summertime precipitation over the Central
2 Andes, *Monthly Weather Review*, *127*(5), 901-919.

3 Hansen, P. C., et al. (1992), The modified truncated SVD method for regularization in general
4 form, *SIAM Journal of Scientific Computing*, *13*(5), 1142-1150.

5 Heck, B. (1990), An evaluation of some of the systematic error sources affecting terrestrial
6 gravity anomalies, *Journal of Geodesy*, *64*(1), 88-108.

7 Heiskanen, W. A., and H. Moritz (1967), *Physical Geodesy*, 364 pp., W. H. Freeman, San
8 Francisco.

9 Henderson, R. G., and L. Cordell (1971), Reduction of unevenly spaced potential field data to a
10 horizontal plane by means of finite harmonic series, *Geophysics*, *36*(5), 856-866.

11 Hinze, W. J. (2003), Bouguer reduction density, why 2.67?, *Geophysics*, *68*(5), 1559-1560.

12 Hwang, C. (1993), Spectral analysis using orthonormal functions with a case study on the sea
13 surface topography, *Geophysical Journal International*, *115*(3), 1148-1160.

14 James, W. R. (1966), Fortran IV program using double Fourier series for surface fitting of
15 irregularly spaced data, *Computer Contributions, Kansas State Geological Survey*, *5*, 19.

16 Jekeli, C., and J. G. Serpas (2003), Review and numerical assessment of the direct topographical
17 reduction in geoid determination, *Journal of Geodesy*, *77*(3-4), 226-239.

18 Katz, D. M., et al. (1995), Effects of surface roughness and rainfall impact on overland flow,
19 *Journal of Hydraulic Engineering*, *121*(7), 546-553.

20 Kaufman, D. W. (1960), Physical Properties of Sodium Chloride in Crystal, Liquid, Gas, and
21 Aqueous Solution States, in *Sodium Chloride: The Production and Properties of Salt and Brine*,
22 edited by D. W. Kaufman, p. 743, Reinhold Publishing Corporation, New York.

23 Lemoine, F. G., et al. (1998), The development of the joint NASA SDFC and the National
24 Imagery and Mapping Agency (NIMA) geopotential model EGM96, 575 pp, GSFC, Greenbelt,
25 Maryland.

26 Lide, D. R. (Ed.) (2007), *CRC Handbook of Chemistry and Physics*, 88 ed., 2640 pp., CRC
27 Press, Cleveland, Ohio.

28 Lowenstein, T. K., and L. A. Hardie (1985), Criteria for the recognition of salt-pan evaporites,
29 *Sedimentology*, *32*(5), 627-644.

30 MacCormack, R. W. (1971), Numerical solution of the interaction of a shock wave with a
31 laminar boundary layer, in *Second Internation Conference on Numerical Methods in Fluid*
32 *Dynamics*, edited, pp. 151-163, New York: Springer, University of California, Berkeley.

McGeary, S., et al. (2003), Shallow seismic reflection imaging of the salar de Uyuni, Bolivia: Quaternary neotectonics and stratigraphy, in *Eos Trans. AGU*, edited, pp. T32E-05, San Francisco, CA.

Menking, K. M., et al. (2000), Evaporation from groundwater discharge playas, Estancia Basin, central New Mexico, *Global and Planetary Change*, *25*(1), 133-147.

NIMA (1997), Department of Defense World Geodetic System 1984: Its Definition and Relationships with Local Geodetic Systems (TR 8350.2-B), 171 pp, National Imagery and Mapping Agency.

Pail, R., et al. (2001), Spatially restricted data distributions on the sphere: the method of orthonormalized functions and applications, *Journal of Geodesy*, *75*(1), 44-56.

Ponce, V. M., et al. (1978), Applicability of kinematic and diffusion models, *Journal of the Hydraulic Engineering*, *104*(3), 352-360.

Rabus, B., et al. (2003), The shuttle radar topography mission - a new class of digital elevation models acquired by spaceborne radar, *Photogrammetry and Remote Sensing*, *57*(4), 241-262.

Rettig, S. L., et al. (1980), Geochemical Evolution of Brines in the salar of Uyuni, Bolivia, *Chemical Geology*, *30*, 57-79.

Risacher, F., and S. C. Fritz (2000), Bromine geochemistry of salar de Uyuni and deeper salt crusts, Central Altiplano, Bolivia, *Chemical Geology*, *167*(3), 373-392.

Schreiber, B. C., and M. El Tabakh (2000), Deposition and early alteration of evaporites, *Sedimentology*, *47*(s1), 215-238.

Schwarz, K. P., et al. (1990), The use of FFT techniques in physical geodesy, *Geophysics Journal International*, *100*, 485-514.

Sideris, M. G., and Y. C. Li (1993), Gravity field convolutions without windowing and edge effects, *Journal of Geodesy*, *67*(2), 107-118.

Simon, B. (1981), Dissolution rates of NaCl and KCl in aqueous solution, *Journal of Crystal Growth*, *52*(2), 789-794.

Sonnenfeld, P. (1984), *Brines and Evaporites*, 1 ed., 613 pp., Academic Press, Orlando.

Tyler, S. W., et al. (1997), Estimation of groundwater evaporation and salt flux from Owens Lake, California, USA, *Journal of Hydrology*, *200*(1), 110-135.

Vreugdenhil, C. B. (1994), *Numerical Methods for Shallow-Water Flow*, 1 ed., 261 pp., Kluwer Academic Publishers, Dordrecht; Boston.

Warren, J. K. (1989), *Evaporite Sedimentology*, 1 ed., 285 pp., Prentice-Hall, Inc., Englewood Cliffs.

Xu, P. (1998), Truncated SVD methods for discrete linear ill-posed problems, *Geophysical Journal International*, *135*(2), 505-514.

Zhang, W., and T. W. Cundy (1989), Modeling of two-dimensional overland flow, *Water Resources Research*, *25*(9), 2019-2035.

FIGURE CAPTIONS

Figure 1. True-color MODIS image of the salar de Uyuni and environs in the Central Andes. The salar is approximately 100 km across and sits at the low point of an internal-drainage basin that covers most of the image area within the borders of Bolivia. Its surface is almost pure halite (sodium chloride) and appears bright white during the dry season.

Figure 2. LANDSAT scene of the salar de Uyuni and surrounding region (200 x 200 km). Station locations from the YPFB gravity survey are plotted as + symbols, with those in orange marking the 10873 stations used in this study. The 45 × 54 km region covered by the GPS DEM is shaded in black. All figures in this paper, unless otherwise indicated, are oriented north-south.

Figure 3. Contour plot of the direct topographic effect on gravity in the salar de Uyuni region (2 mGal contours in blue, 10 mGal contours in green). Over this area, the direct effect ranges from 0.016 mGal to 39 mGal, with the largest values associated with the stratovolcanos surrounding the salar. On the salar itself, the direct effect is negligible.

Figure 4a. Contour plot of the $A = B = 16$ harmonic expansion model for the residual Helmert gravity anomaly data on the salar de Uyuni (2 mGal contours). Data locations are plotted in orange and are generally confined to the salar and the flatter surrounding terrain, with gaps at the edges of the data window and in areas of high topographic relief. The model misfit is only 0.96 mGal RMS, but the extreme amplitudes of the model within the data gaps (up to 10^9 mGal) indicates that it poorly represents the underlying gravity anomaly field.

Figure 4b. Harmonic expansion model of salar de Uyuni residual Helmert anomaly, truncated from 1088 to 478 terms (2 mGal contours). Although model misfit increases to 1.85 mGal and some shorter-wavelength features are lost, the artifacts of the original model outside the data are heavily damped.

Figure 5. Plot of SVD-truncated model misfit versus the size of the model coefficient vector c_k, with varying truncation level k. An approximate balance between model size and misfit is obtained at the maximum curvature point of the plot, which corresponds to the truncation of the 1088 terms in the original model to 478 terms (i.e., $k = 610$).

Figure 6. The equipotential surface corresponding to the Helmert gravity anomaly model in Figure 4b (2.5 cm contours). The dominant feature is the central plateau, which corresponds to the broad high in the Helmert model and which stretches across the western portion of the GPS survey area. The elongated depression running SW-NE crosses the southern portion of the GPS survey. Short-wavelength features in the Helmert model are almost completely erased by the wavenumber division that yields the equipotential surface.

Figure 7a. Topography of the salar de Uyuni from GPS (*DEM*). The surface has a standard deviation about the mean of 12.9 cm and a range of 69 cm. Elevations in figures 7~10 are identically scaled according to the color bar shown. **Figure 7b.** The EGM96 equipotential surface (*A*) corresponding to 7a, showing the similarity in the overall slopes of the topography and the equipotential field.

Figure 8a. The topographic residual (*DEM minus A*) obtained by removing the EGM96 surface in 7b from the topography in 7a. Its standard deviation is 9.4 cm and range is 42 cm. **Figure 8b.** The best-fitting plane (*B*) to the residual surface in 8a. This plane is a proxy for error at wavelengths longer than the distance across the DEM.

Figure 9a. The detrended residual (*DEM minus A+B*) obtained by removing the plane in 8b from the residual topography in 8a. Its standard deviation is 7.8 cm and range is 34 cm. **Figure 9b.** The equipotential surface (*C*) derived in this paper from local gravity measurements, detrended to remove long-wavelength error.

Figure 10a. The short-wavelength topography (*DEM minus A+B+C*) remaining after removing the local equipotential surface in 9b from the detrended residual in 9a. Its standard deviation is 3.5 cm and range is 19 cm, showing that most of the variance in the original DEM has been removed. **Figure 10b.** An independent estimate of surface height relative to the local equipotential surface, obtained using water depth estimates from a single MISR image. The residual difference between 10a and 10b has a standard deviation of only 2.4 cm.

Figure 11a. Composite model of the gravitational equipotential surface over the salar de Uyuni, formed from the sum of components *A*, *B* and *C* from figures 7b, 8b and 9b. The elevation color scale is the same as in figures 7~10. **Figure 11b.** The salar DEM, for comparison with the model in Figure 11a.

Figure 12. Percentage saturation with time of a well-mixed water column of height *a* over a pure halite surface (c.f. Equation 28). An initially-pure water column of 1 cm takes 1.5 h to reach 95% saturation, while a 2 cm column takes about 3.5 hours.

Figure 13. Rainfall recorded at Oruro, Bolivia for the period July, 2002 ~ June, 2003. Total precipitation was 29.5 cm, most of which occurred in the rainy season between December and March.

Figure 14. Location of the topography transect (A-AA) used for overland flow modeling. We use topography from the geoid-referenced DEM of the salar de Uyuni, since gravity-driven water flow is related to water height above the geoid rather than above the ellipsoid.

Figure 15a. Initial rainfall of 2 centimeters, distributed as a uniform surface layer. **Figure 15b.** After 2 days, overland flow has filled low-lying areas, with continuing downslope water movement from higher areas. **Figure 15c.** After 5 days, sloping surfaces are generally dry and ponded water has begun to evaporate.

Figure 16a. Modeled evolution of the topography transect A-AA due to salt transport on the salar by overland flow of rainwater, with evaporation rate set at 2.0 mm/day. Profiles are at one-year increments from 0 years (lightest grey) to 10 years (black). **Figure 16b.** Same as 16a, but with the evaporation rate set to 2.5 mm/day.

TABLES

Table 1. Topography modeling results. The first row shows statistics for the salar de Uyuni DEM described in Section 2.1, and subsequent rows show the changes due to subtracting various components of modeled topography (A = EGM96 equipotential surface, B = planar error estimate, C = equiptotential surface derived in this paper).

	Elevation Range	Standard Deviation (σ)	Variance	% Original Variance
GPS-derived DEM	69.6 cm	12.9 cm	166 cm^2	100%
DEM minus A	41.8 cm	9.4 cm	88 cm^2	53%
DEM minus A+B	33.7 cm	7.8 cm	61 cm^2	37%
DEM minus A+B+C	19.0 cm	3.5 cm	12 cm^2	7%

1 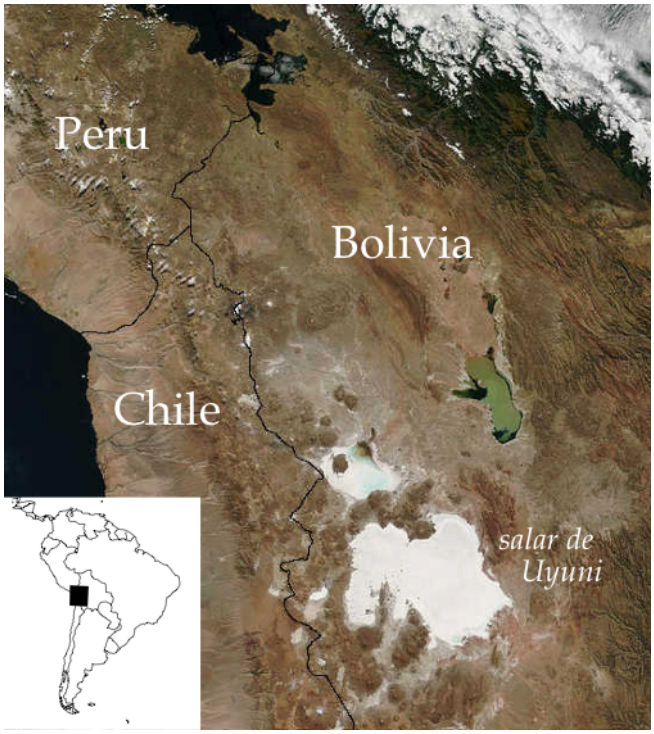

2 Figure 1.

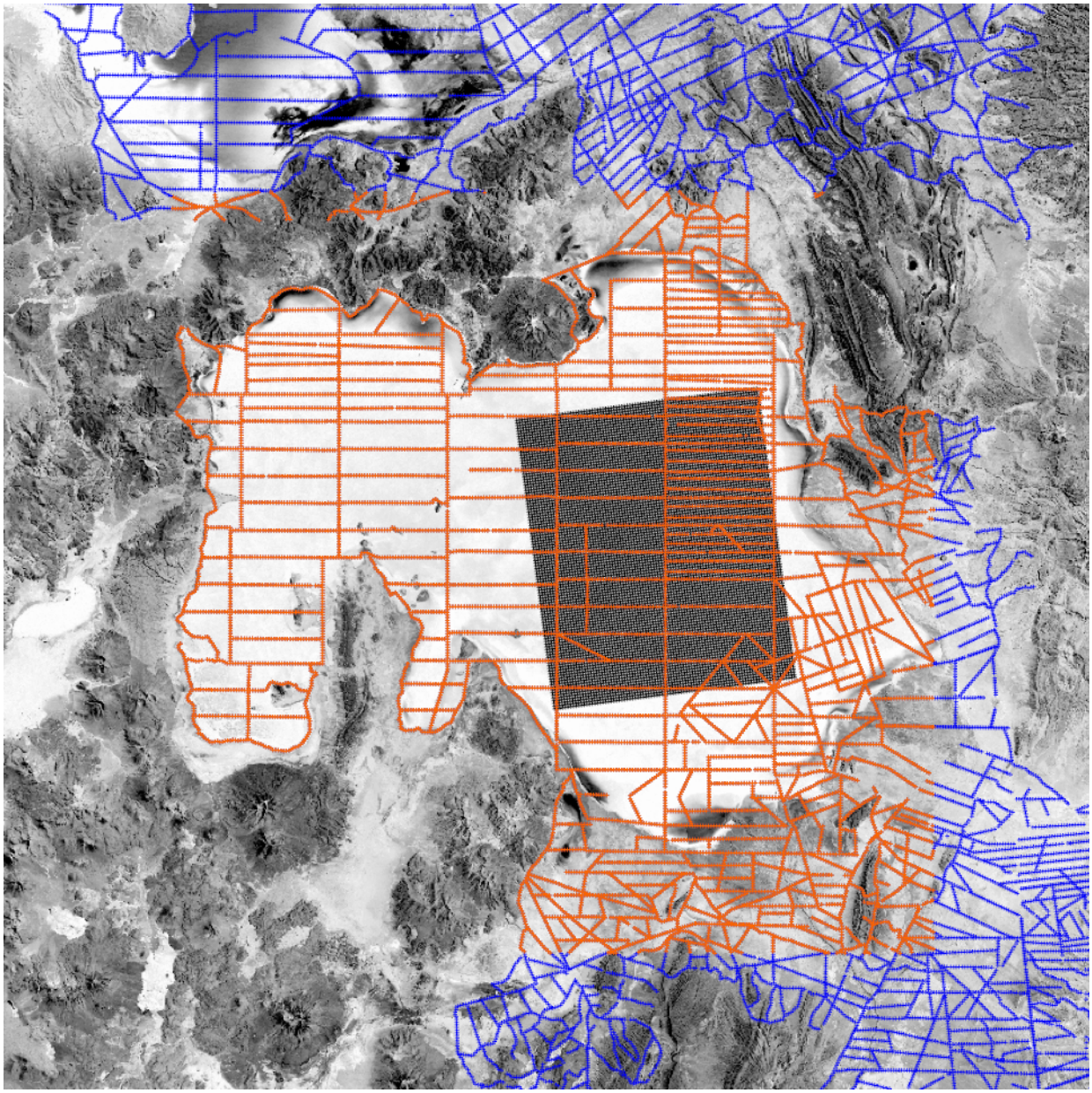

Figure 2.

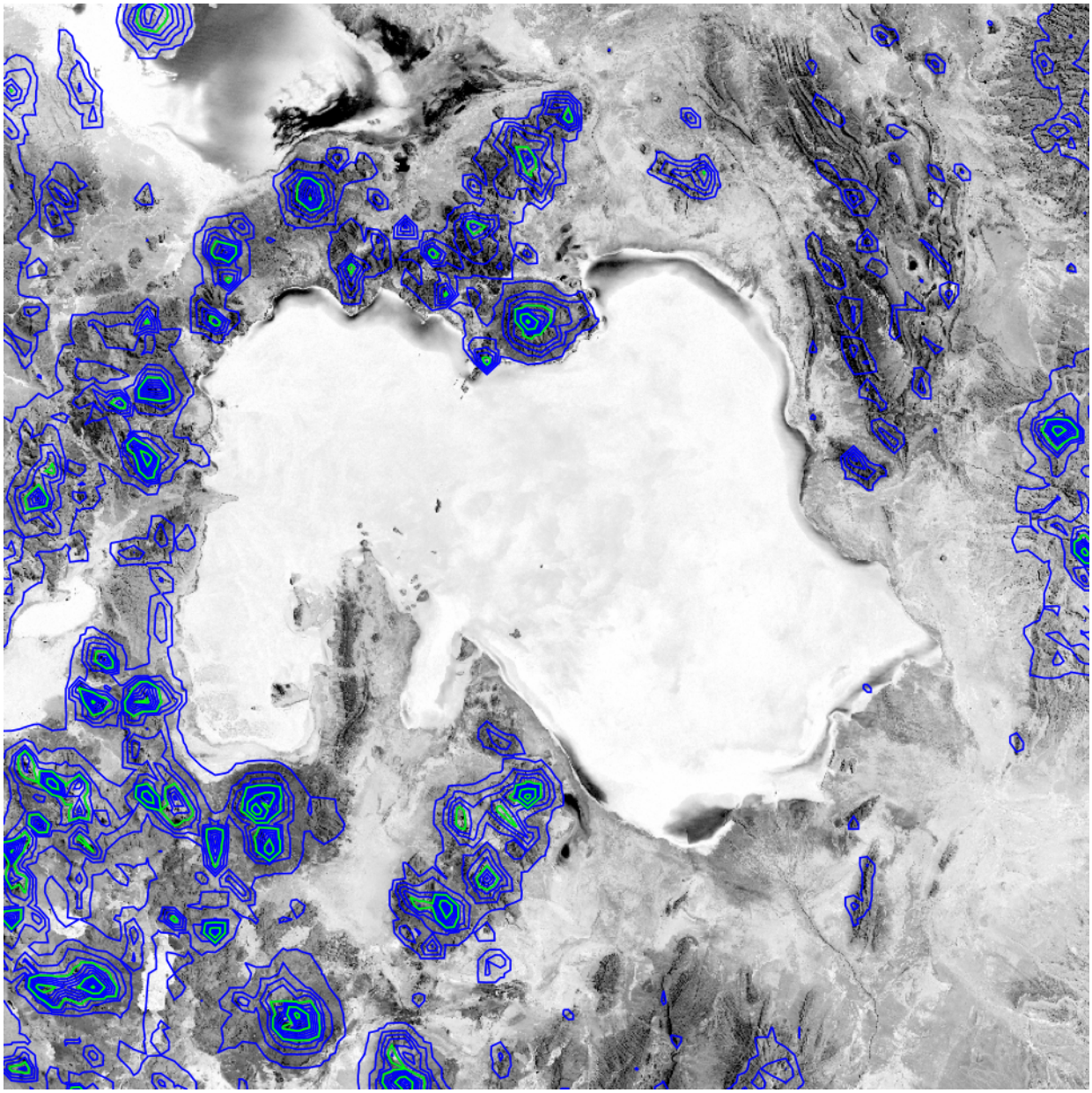

Figure 3.

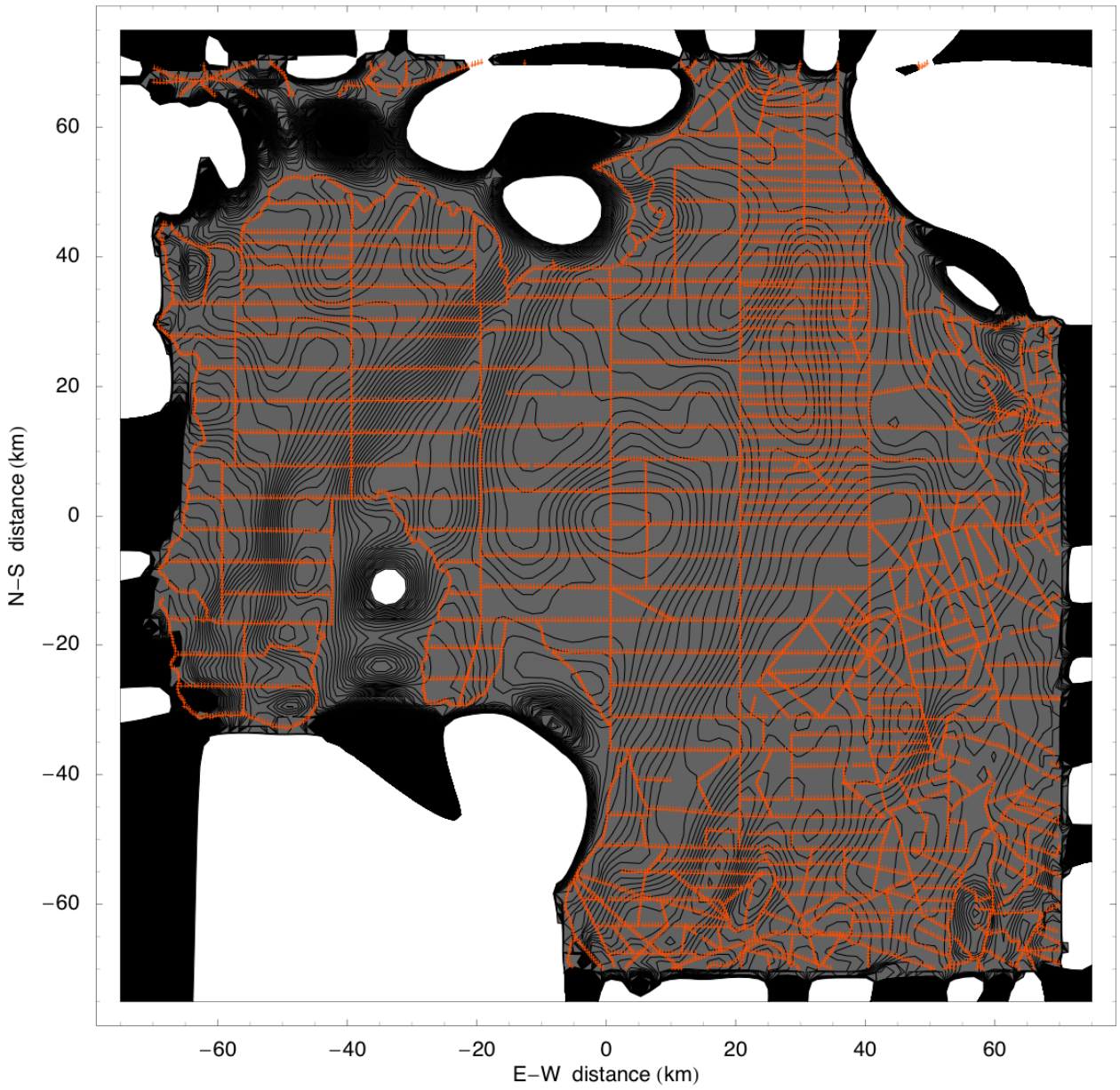
60
40
20
0
−20
−40
−60
N−S distance (km)
−60
−40
−20
0
20
40
60
E−W distance (km)

1

2 Figure 4a.

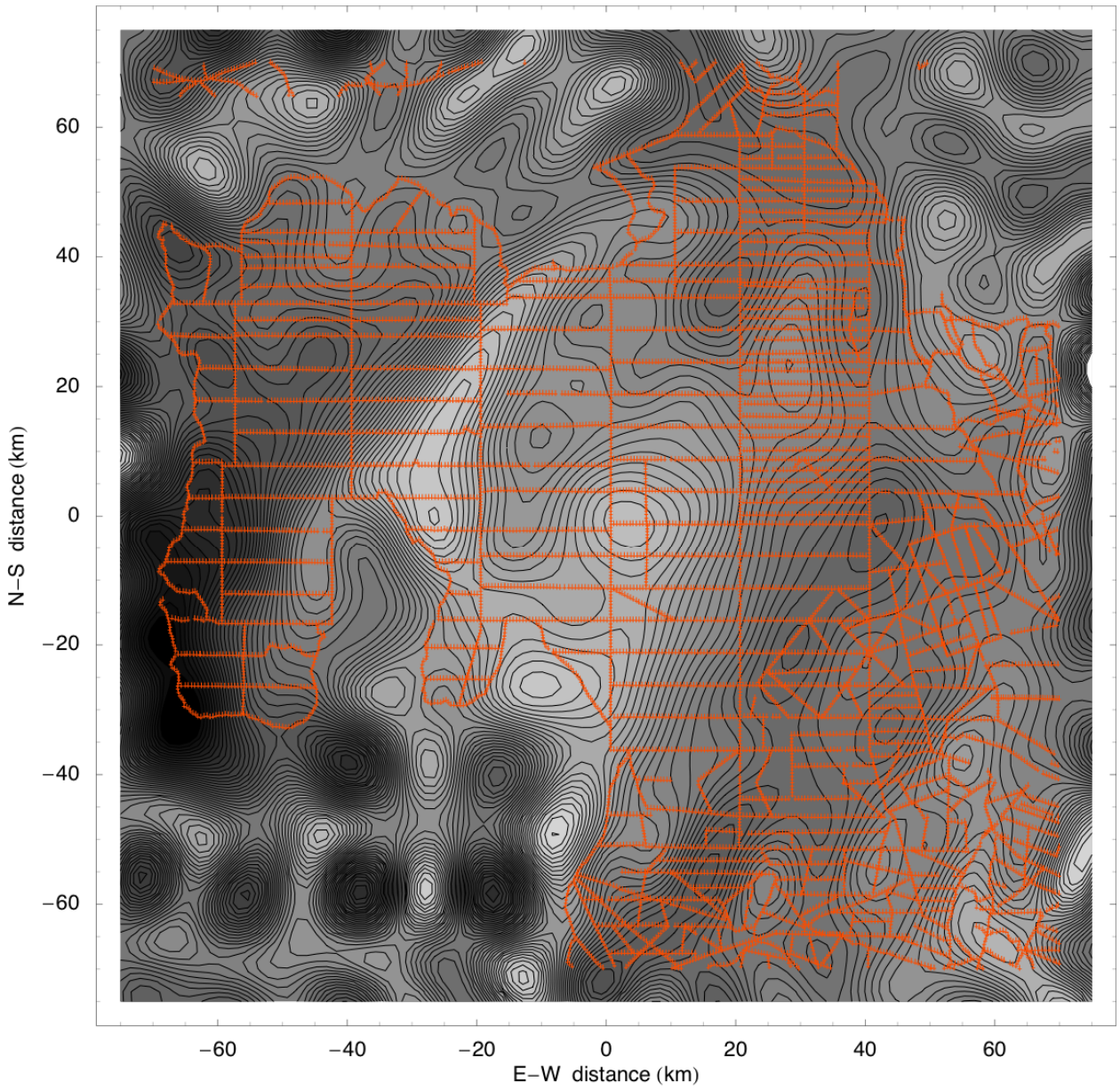
60
40
20
0
−20
−40
−60
N−S distance (km)
−60
−40
−20
0
20
40
60
E−W distance (km)

1

2 Figure 4b.

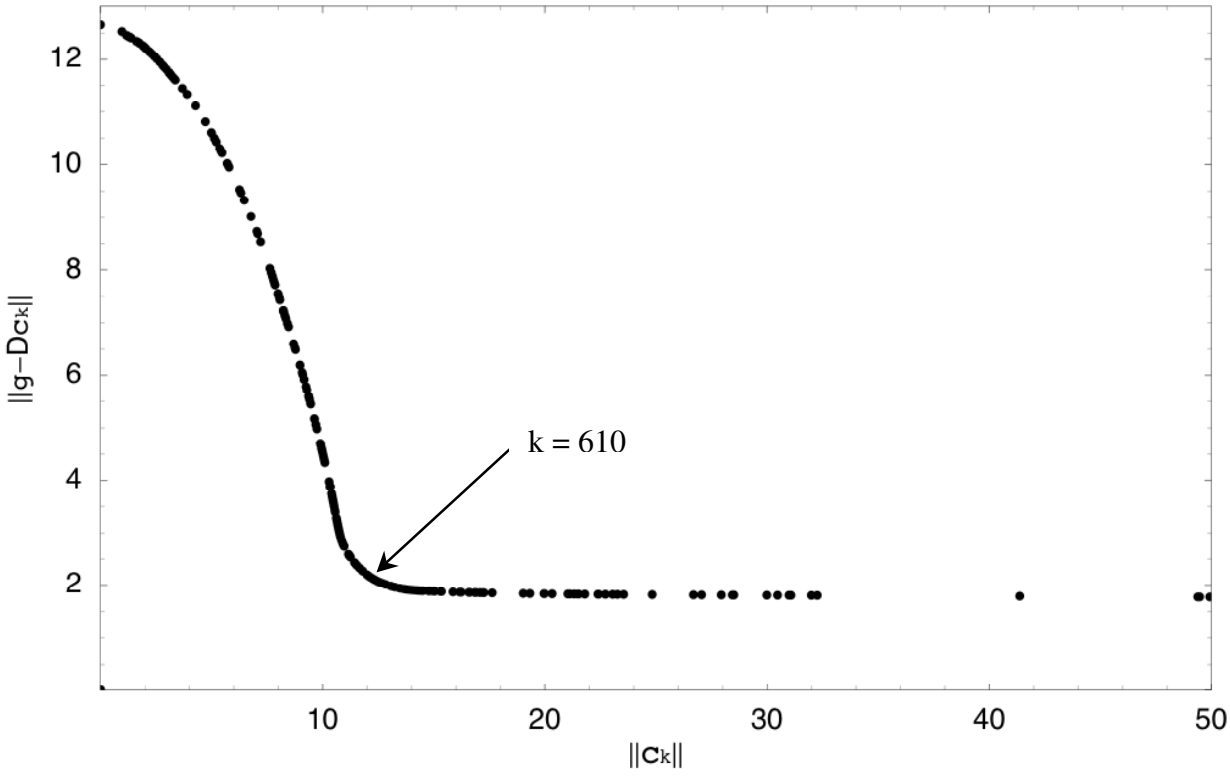

Figure 5.

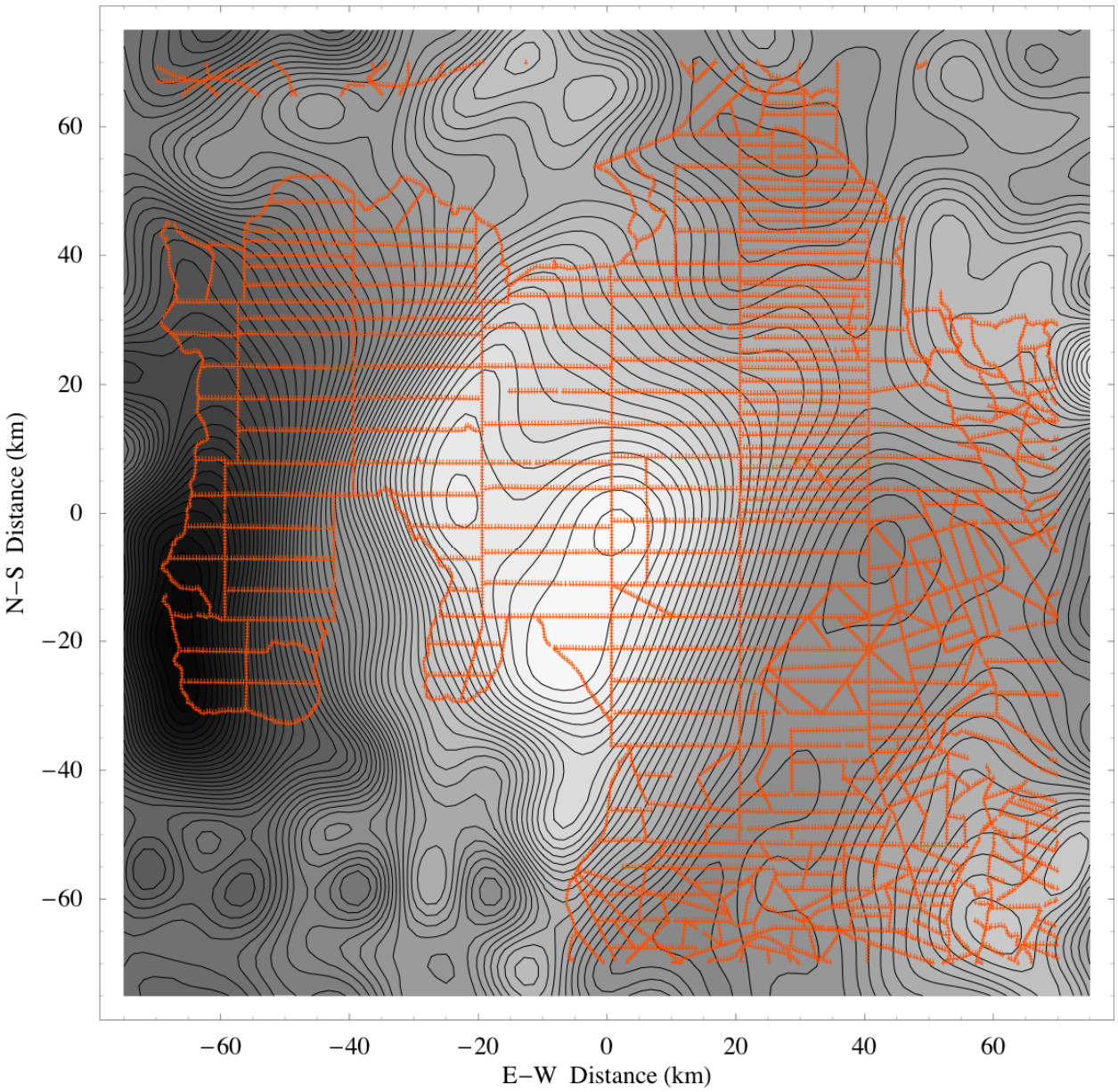
60
40
20
0
−20
−40
−60
N−S Distance (km)
−60
−40
−20
0
20
40
60
E−W Distance (km)

1

2 Figure 6.

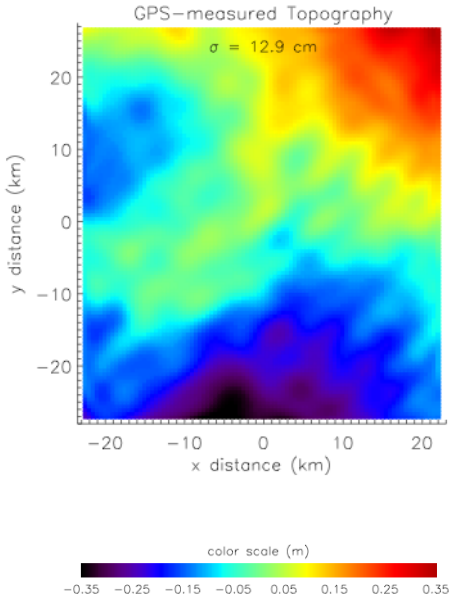

1

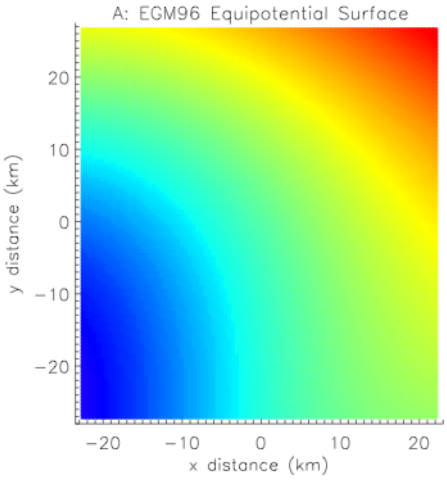

2

3 Figure 7a. Figure 7b.

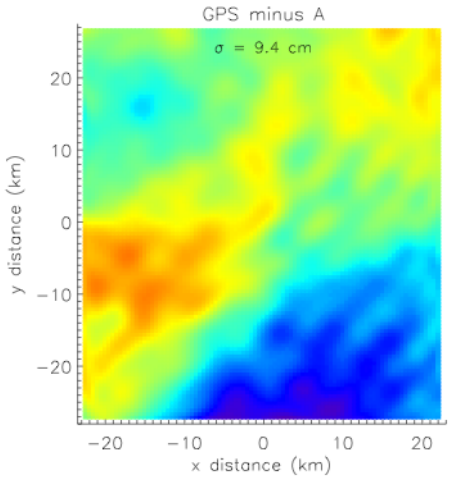

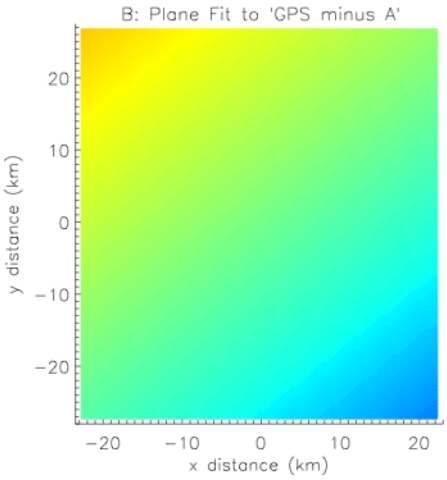

4

5 Figure 8a. Figure 8b.

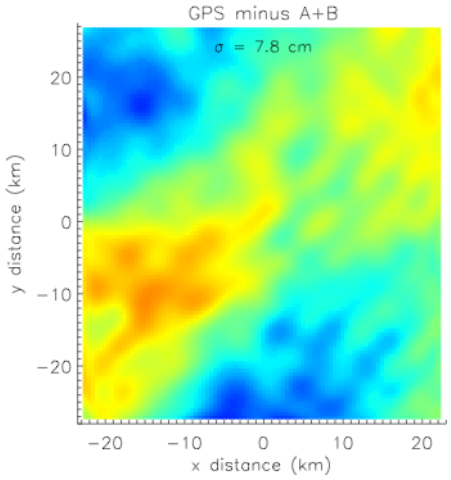

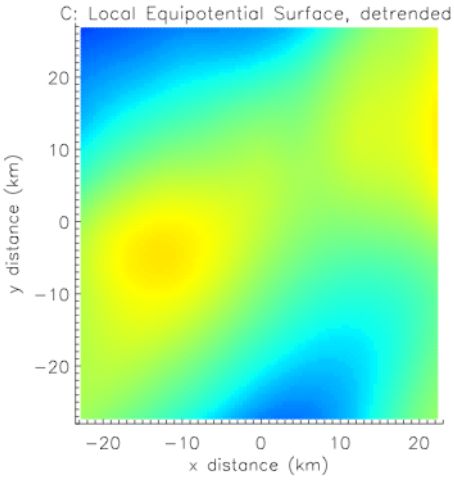

1

2 Figure 9a. Figure 9b.

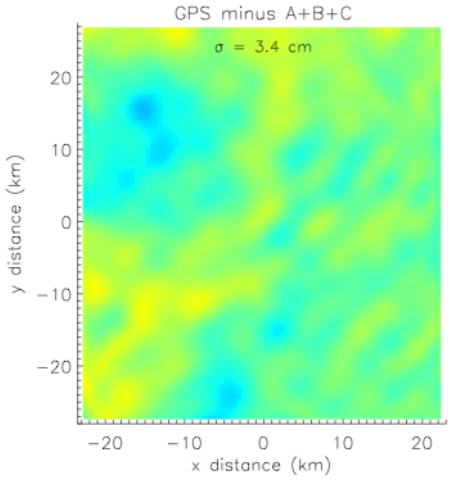

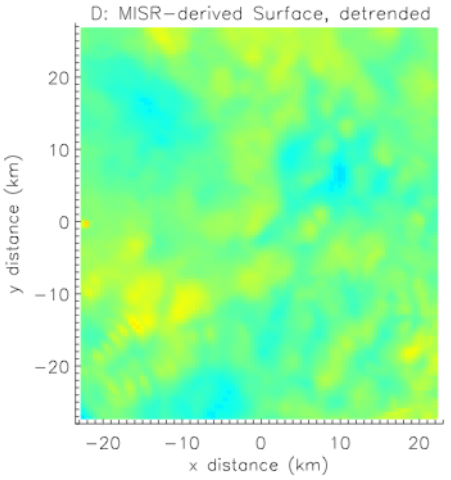

3

4 Figure 10a. Figure 10b.

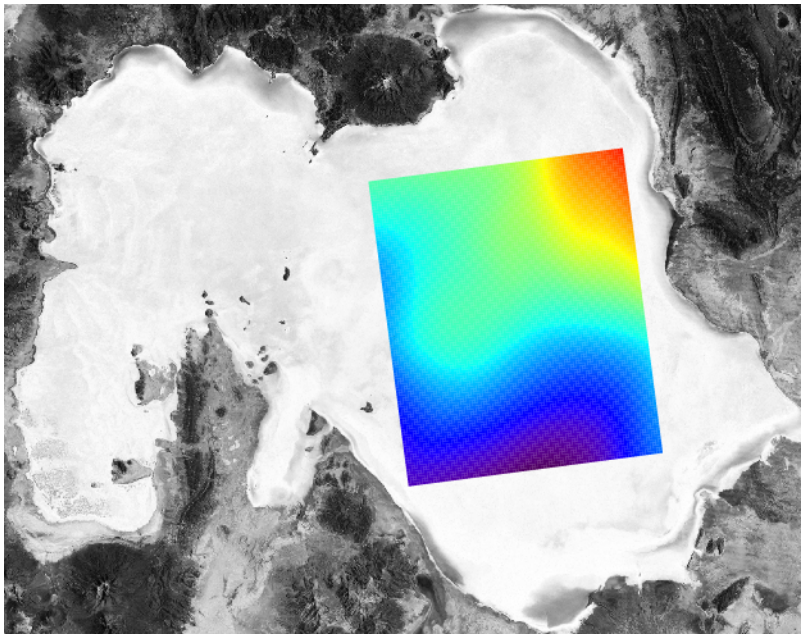

Figure 11a.

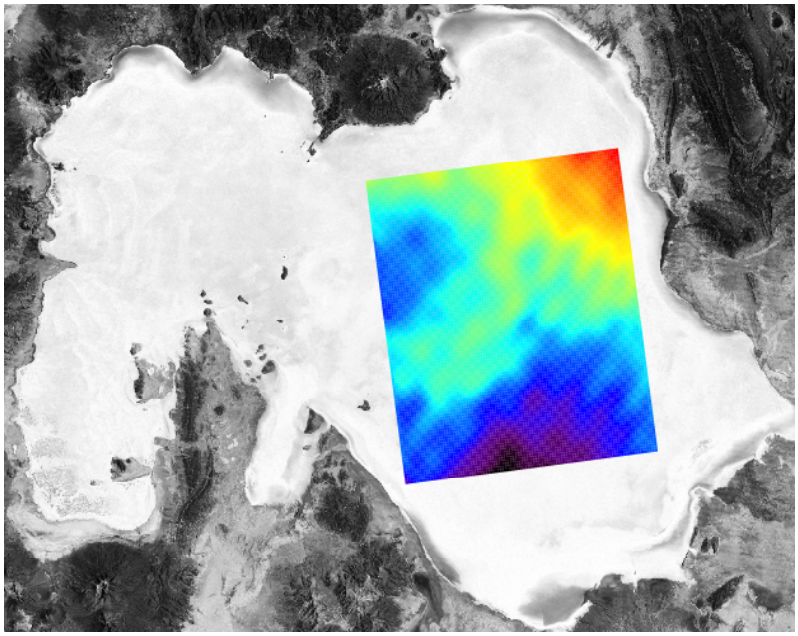

Figure 11b.

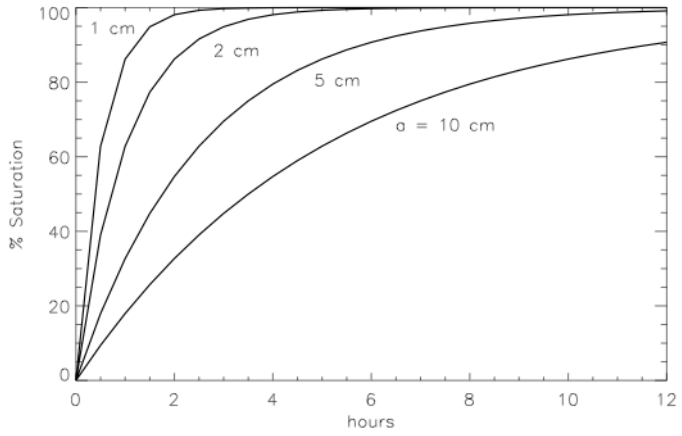
100
80
60
40
20
0
% Saturation
1 cm
2 cm
5 cm
a = 10 cm
0
2
4
6
8
10
12
hours

1

2 Figure 12.

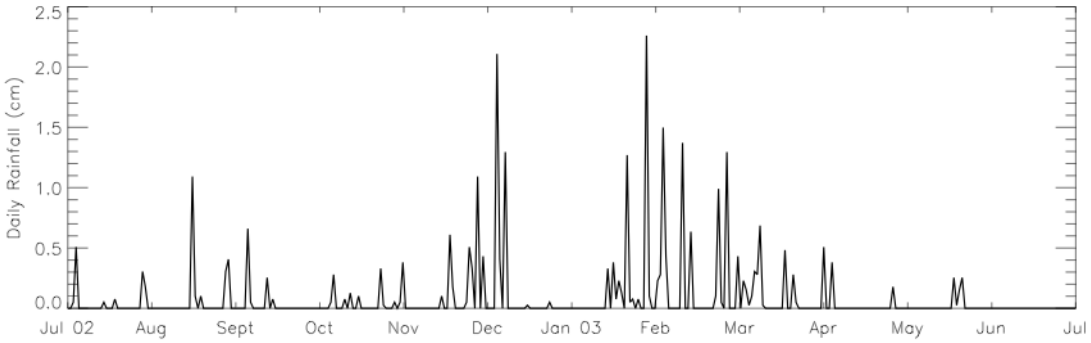
Daily Rainfall (cm)
2.5
2.0
1.5
1.0
0.5
0.0
Jul 02
Aug
Sept
Oct
Nov
Dec
Jan 03
Feb
Mar
Apr
May
Jun
Jul

1

2 Figure 13.

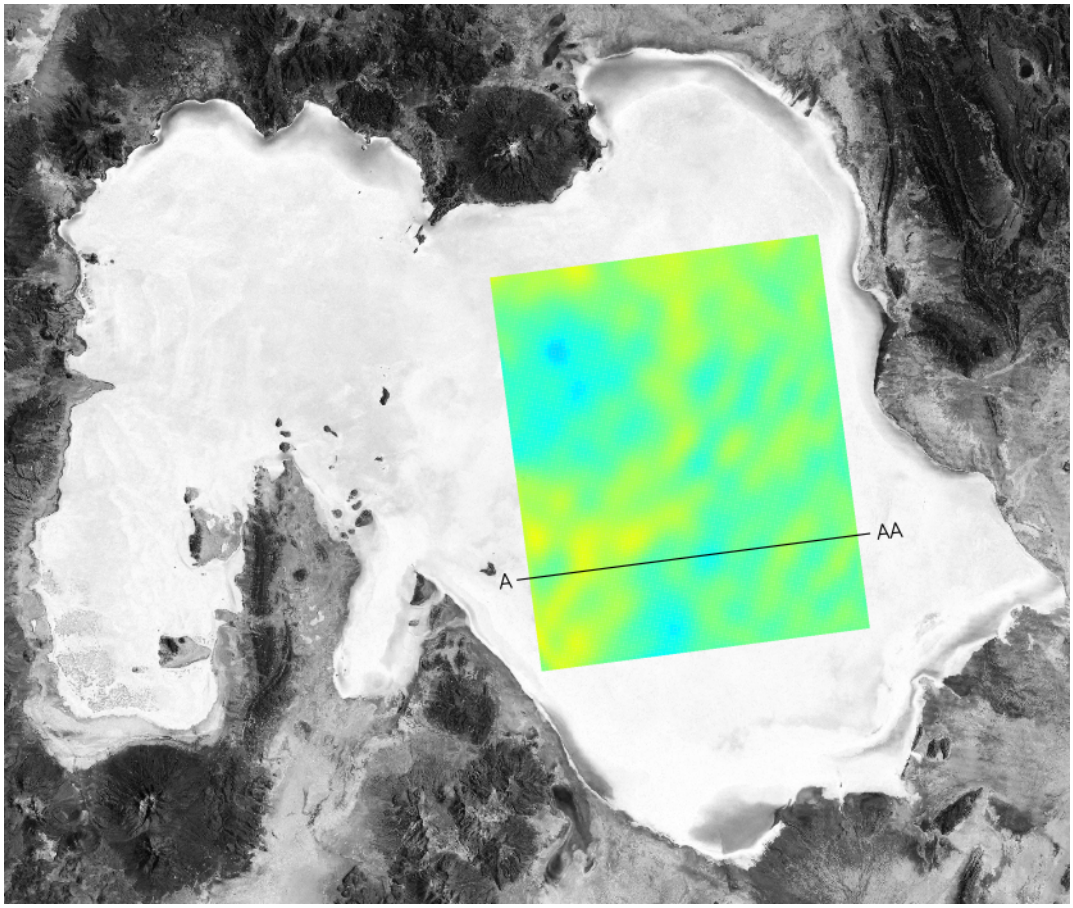

Figure 14.

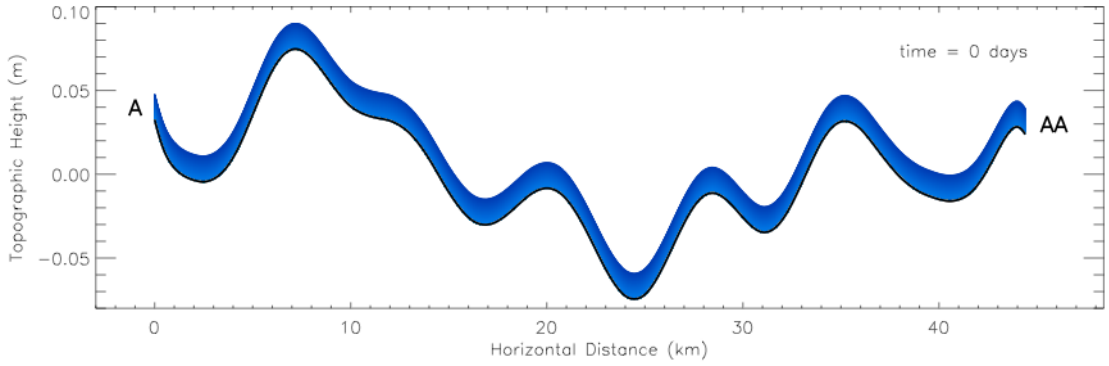

1

2 Figure 15a.

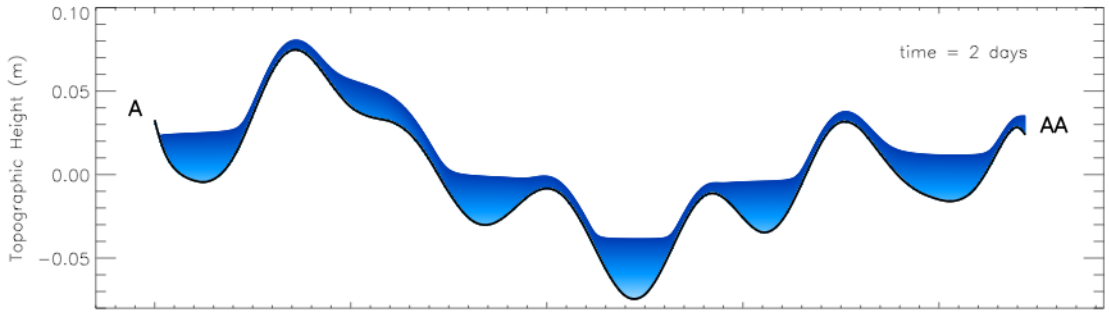

3

4 Figure 15b

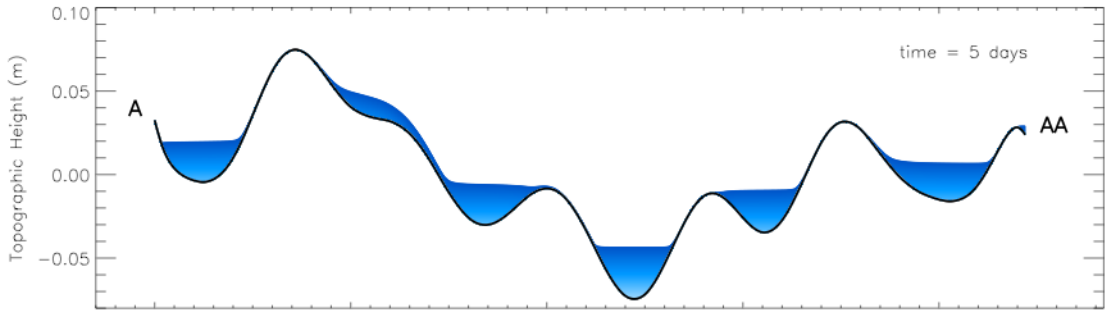

5

6 Figure 15c.

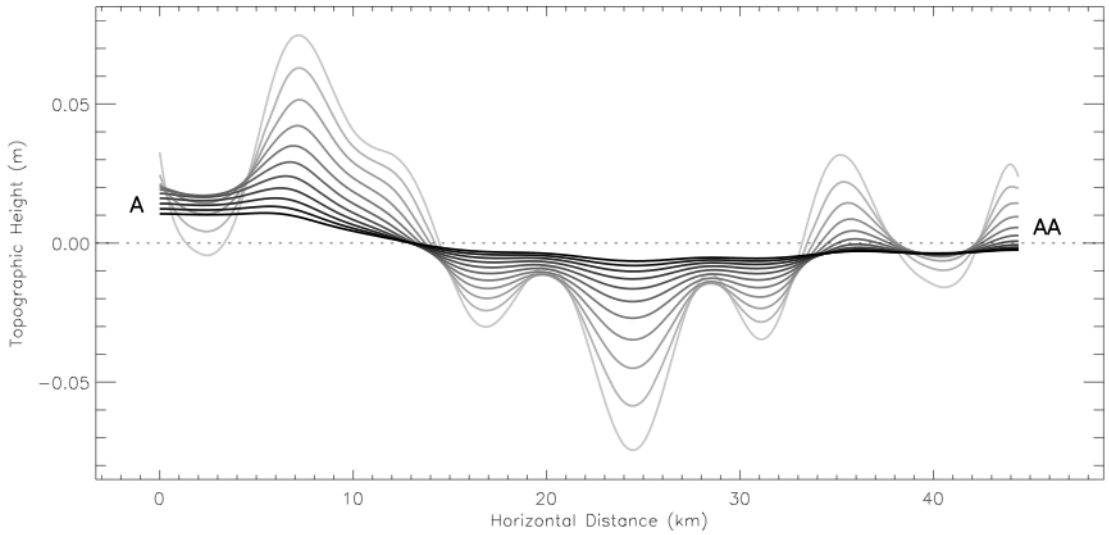

1

2 Figure 16a.

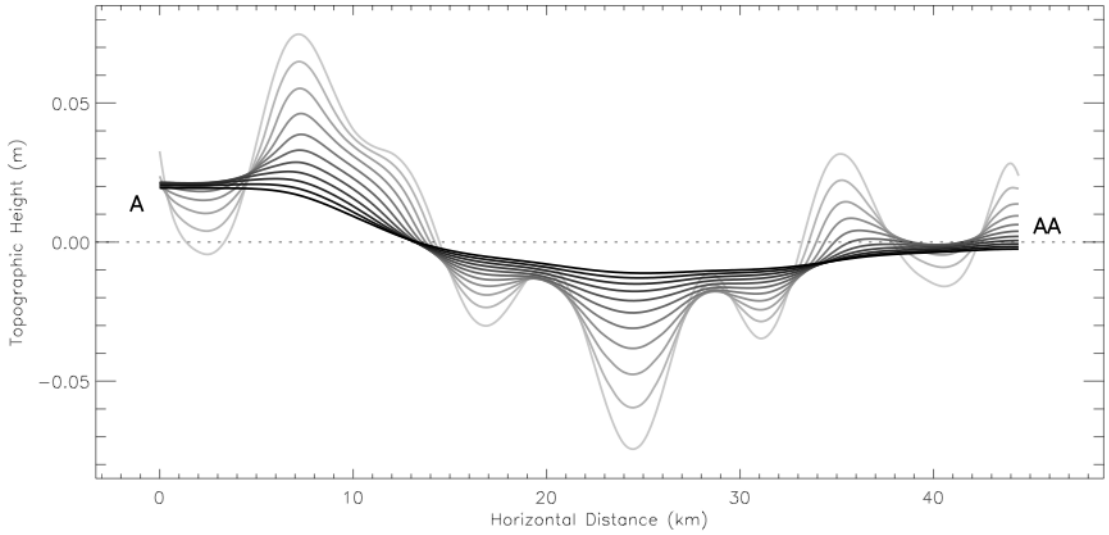

3

4 Figure 16b.